Soft Materials

ISSN: (Print) (Online) Journal homepage: www.tandfonline.com/journals/lsfm20

Design and self-assembly of new peptides and peptide bolaamphiphiles as antioxidant biocomposite scaffolds for potential tissue regeneration applications – a replica modeling and experimental study

Hannah L. Hunt, Mary A. Biggs, Beatriz G. Goncavles & Ipsita A. Banerjee

To cite this article: Hannah L. Hunt, Mary A. Biggs, Beatriz G. Goncavles & Ipsita A. Banerjee (06 Nov 2024): Design and self-assembly of new peptides and peptide bolaamphiphiles as antioxidant biocomposite scaffolds for potential tissue regeneration applications – a replica modeling and experimental study, Soft Materials, DOI: 10.1080/1539445X.2024.2413063

To link to this article: https://doi.org/10.1080/1539445X.2024.2413063

SOFT MATERIALS
https://doi.org/10.1080/1539445X.2024.2413063

Taylor & Francis
Taylor & Francis Group

Design and self-assembly of new peptides and peptide bolaamphiphiles as antioxidant biocomposite scaffolds for potential tissue regeneration applications – a replica modeling and experimental study

Hannah L. Hunt, Mary A. Biggs, Beatriz G. Goncavles, and Ipsita A. Banerjee

Department of Chemistry and Biochemistry, Fordham University, Bronx, New York, USA

ABSTRACT

In this work, five new peptides derived from natural resources and two peptide bolaamphiphiles were designed. The self-assembling ability of the peptides and the bolaamphiphiles, as well as their predicted antioxidant activity was examined computationally. In particular, replica modeling molecular dynamics studies were carried out at three different temperatures. Results showed that the bolaamphiphiles as well as three of the peptides efficiently formed spherical or fibrous assemblies, particularly at physiological temperatures. In addition, stacking interactions and hydrogen bonds played a critical role in assembly formation. Furthermore, molecular docking studies with extracellular matrix proteins such as the triple helix motif of collagen and the fibronectin (III) motif of tenascin-X displayed binding interactions with the peptides and the bolaamphiphiles. The most optimal peptide bolaamphiphile WMYGGGWMY-CO-NH-$(CH_2)_4$-YMWGGGYMW was then synthesized in the laboratory and its ability to form functional scaffolds upon binding to collagen and tenascin-X was examined. The scaffolds were bioprinted with co-cultures of fibroblasts and keratinocytes. The cells not only proliferated over time but also showed strong adherence and spreading within the matrix. Thus, the peptides and the bolaamphiphiles studied in this work, may be potentially developed as scaffold components for tissue regeneration applications.

ARTICLE HISTORY
Received 21 July 2024
Accepted 1 October 2024

KEYWORDS
Replica modeling; tissue regeneration; peptides; antioxidant; scaffold

Introduction

Self-assembling biomaterials have gained immense popularity over the years due to their ability to form intricate structures that can be fine-tuned for specific biological applications.[1] A wide variety of self-assembling systems have been investigated for applications in targeted drug delivery, wound healing, tissue regeneration, or in the development of artificial cell networks.[2–4] In particular, self-assembling biological systems such as lipids, nucleic acids, phytochemicals, peptides, or carbohydrates and other biopolymers have been utilized to form unique nano and microscale architectures by controlling the growth conditions such as temperature, pH, ionic strength, and solvent systems.[5–7] Furthermore, functionalization of the nano and microscale materials allows for developing biomaterials that can mimic the natural extracellular environment and provide biological cues for cell signaling. In addition, hybrid bio-organic materials such as carbohydrate and peptide based amphiphiles or bolaamphiphiles have also gained importance in this area due to their facile self-assembly, stability, and their ability to form biocompatible scaffolds.[8,9] Over the years, it has been reported that computational studies can provide key insights into the self-assembling ability of newly designed biomimetic molecules and the interactions involved therein.[10,11] change to[10–14] For example, in a recent study it was shown through atomistic molecular dynamics (MD) simulations that the phospholipid, Dipalmitoylphosphatidylcholine (DPPC) could spontaneously self-assemble and form a complex with model hydrophobic peptides and that the aggregation process occurred in a stepwise manner.[15] In another study, generative deep learning and molecular dynamics simulations were utilized to design protein-specific inhibitors to target β-catenin and NF-κB modulators.[16]

In addition to molecular docking studies, all-atom MD simulations are beneficial as they can account for the flexibility of proteins as well as predict relatively accurate binding poses over the simulation time.[17–19] However, it is arduous to examine peptide–protein interactions adequately through traditional standard MD simulations because of relatively slow dynamics and lower simulation times. Notably, to obtain better convergence, enhanced sampling or an ensemble

CONTACT Ipsita A. Banerjee banerjee@fordham.edu Department of Chemistry and Biochemistry, Fordham University, 441, East Fordham Road, Bronx, New York 10458, USA.
Supplemental data for this article can be accessed online at https://doi.org/10.1080/1539445X.2024.2413063.

methodology such as Replica Exchange Molecular Dynamics (REMD) may be preferred. In particular, T-REMD involves multiple independent simulations run at different temperatures[20] and has been shown to improve predictions of binding interactions. In T-REMD, replicas of the same system are simulated at varying temperatures in parallel MD simulations. Thus, a replica at one temperature may exchange with that at another temperature where energy barriers may be different; thereby increasing the sampling of each replica. T-REMD, thus can potentially overcome high-energy barriers and sample conformational spaces more efficiently.[21] For example, in a study conducted for the first 12 residues of the protein alpha-synuclein (ASyn-12) using T-REMD simulations it was shown that the A-syn12 peptide adopted four different conformational states in water and that the conformations were dependent upon solvent exposure of hydrophobic residues in the secondary structure.[22] In a separate study, REMD simulations performed on various mutated forms of the protein M-crystallin revealed that the mutations caused changes in the secondary structures, and led to increased movement in the N-terminal of the protein, thereby disrupting interactions that resulted in different folded and partially unfolded states.[23]

In this work, we designed and investigated the self-assembly of five peptides and two peptide bolaamphiphiles. The peptide sequences were designed by either modifying known peptide sequences with antioxidant properties obtained from naturally derived sources[24–26] or by creating chains of repeated sequences of peptides using amino acids that are known to impart antioxidant properties to proteins.[27] In addition, the two peptide bolaamphiphiles that were designed contained two of the antioxidant peptides as head groups, connected by a C4 hydrophobic tail. The chemical constituents of the designed peptides and the peptide bolaamphiphiles are shown in Table 1. We specifically designed peptides with antioxidant properties as those may have anti-inflammatory properties, along with free-radical scavenging activity, and therefore may be more biologically desirable for a variety of applications such as in tissue regeneration or drug delivery.[28] The antioxidant activity of the newly designed peptides was predicted using the AnOXPePred web server.[29] The ability of the bioactive peptides and the peptide bolaamphiphiles to form supramolecular assemblies was explored using T-REMD simulations. Based on the results obtained, we then examined the ability of the peptides and peptide bolaamphiphiles to interact with the triple helix region of extracellular matrix (ECM) proteins collagen II and the fibronectin III domain of Tenascin-X through molecular docking and MD simulations. Because collagen II is a major component of connective tissue,[30] it is often utilized as a constituent of biomaterials for tissue engineering.[31] Collagen-based scaffolds are beneficial as they are highly biocompatible, biodegradable, and have regenerative properties when combined with supporting biomaterials.[32] Collagen is generally structured as tightly packed polyproline II-type helices within a right-handed triple helix that involves a repeat of XaaYaaGly amino acid sequence, contributing to the strong and stable mechanical properties of the protein, where X and Y are usually proline and hydroxyproline.[33]

Tenascin-X is another ECM protein that is known to regulate the spacing of collagen fibrils, and thereby contributes to the structural integrity of connective tissues =, as well as regulates cell adhesion to the ECM.[34] Furthermore, Tenascin X (TN-X) deficiencies have been implicated in Ehlers Danlos Syndrome (EDS) that has similar symptoms of classical EDS such as joint hypermobility, easy bruising, and hyper-elastic skin.[35,36] Thus, docking studies were carried out with the triple helix region of collagen and with the fibronectin type III (FN III) domain of tenascin-X. We hypothesized that by creating supramolecular assemblies with antioxidant properties and forming cross-linked scaffolds of collagen and tenascin-X, may lead to new biocompatible scaffolds with potential applications in tissue regeneration applications. Thus, based on the computational studies, as a proof of concept, one of the most optimal peptide bolaamphiphile, WMYGGGWMY-CO-NH-$(CH_2)_4$-NH-CO-YMWGGGYMW (abbreviated as W-C4-W) was synthesized, self-assembled and cross-linked to collagen and tenascin-X to develop a novel scaffold. The scaffold was bioprinted in the presence of fibroblasts and keratinocytes to examine their potential applicability in potential skin tissue engineering applications. Our results demonstrated that the formed scaffold demonstrated biodegradability and stable mechanical properties. Furthermore, it formed cell-scaffold matrices that

Table 1. Designed peptide sequences and peptide Bolaamphiphiles.

Peptide Sequences
WMYGGGWMY
GADIVA
YYGAEFIF
KYHAGAGHYK
HMWHMWYHMW
Peptide Bolaamphiphiles
WMYGGGWMY-CO-NH-$(CH_2)_4$-NH-CO-YMWGGGYMW
GADIVA-CO-NH-$(CH_2)_4$-NH-CO-AVIDAG

promoted cell proliferation, adhesion and thus may have plausible applications in tissue regeneration applications.

Materials and Methods

Computational Methods

Peptide and Bolaamphiphile Design

Five peptides and two peptide bolaamphiphiles were designed using ChemDraw (20.1.1). The peptides sequences were YYGAEFIF, KYHAGAGAGHYK, HMWHMWYHMW, GADIVA, and WMYGGGWMY. The peptide bolaamphiphiles designed were WMYGGGWMY-CO-NH-$(CH_2)_4$-YMWGGGYMW and GADIVA-CO-NH-$(CH_2)_4$-AVIDAG created by conjugating the terminal carboxyl groups of the two peptides with the amine groups of 1,4 diamino butane. All designed structures were then exported to ChemDraw 3D (20.1.1), followed by MM2 minimization. These 3D structures obtained were then saved as .pdb files and opened on PyMOL (2.5.2)[37] for further processing.

Prediction of Antioxidant Properties of Peptides

In order to explore the antioxidant properties and free radical scavenging ability of the designed peptides, we utilized the AnOxPePred webserver. (https://services.healthtech.dtu.dk/services/AnOxPePred-1.0/). In general, the peptide sequences were input into the webserver in FASTA format. The webserver model consists of curated datasets composed of a range of experimentally tested antioxidant and non-antioxidant peptides and allows for the prediction of free-radical scavenging (FRS) and chelating properties of single peptides and also predicts the activity of peptides within a protein. The output provides specific scores that can be used to predict the antioxidant and chelating ability of peptides.

Determination of Secondary Structural Properties of the Designed Peptides

To determine the individual secondary structural elements of the peptide sequences, two different webservers used, PSSpred and AlphaFold3. The PSSpred (Protein Secondary Structure Prediction) webserver utilizes a neural network training algorithm by collecting multiple sequence alignments using PSI-BLAST. The overall results obtained are determined by coalescing seven neural network predictors based on different profile data and parameters.[38] We also utilized the webserver AlphaFold 3 to determine the secondary structures of the peptide assemblies.[39,40] In general, the FASTA sequences of each of the peptides were uploaded to the server. The number of copies of the sequences was assigned to 30 as we utilized the same for the REMD simulations. The output files obtained demonstrated the structures with colorations indicative of the pLDDT (predicted local distance difference test) scores, ipTM (interface predicted template modeling) scores, which show the precision of the predicted relative positions of the subunits forming the protein–protein complex). Since in our case, we did not examine complexes and no subunits were involved, the ipTM scores were not taken into consideration. The TM (template modeling) scores were also obtained, which examines the accuracy of the entire global structure of the protein and is relatively impervious to local inaccuracies.[41]

Replica Exchange Molecular Dynamics (REMD) of Peptides and Peptide Bolaamphiphiles

In order to determine the self-assembling ability of the designed peptides and peptide bolaamphiphiles, we carried out REMD simulations for which we utilized the Maestro Material Sciences suite (2021–3) platform from Schrödinger.[42] First, the ligands were prepared using the Protein Preparation panel, in which the structure of the ligands were optimized, and the forcefield was set to OPLS_2005. To construct a randomized multi-component system, the Disordered System Builder panel was used. Initially, an orthorhombic periodic boundary condition (PBC) that encompassed the entire system with SPC water model was used. The system's box measured 10 Å × 10 Å × 10 Å and comprised of 30 individual ligands. The placement of each component was randomized to create an amorphous structure that avoided structural clashes by adjusting the position and orientation of each component iteratively. Subsequently, the structure underwent further refinement through energy minimization utilizing the OPLS_2005 force field, resulting in a densely packed disordered system with optimized unit cell dimensions.

The obtained structure was then prepared for replica exchange molecular dynamics (REMD) simulations. Three replicas of the system were concurrently simulated at temperatures of 260 K, 310 K, and 360 K. Prior to commencing the simulations, a materials relaxation protocol was employed, comprising a series of steps: a 100 ps NVT Brownian minimization at 10 K, a 12 ps NVT minimization at 10 K, a 12 ps NPT minimization with restraints on solute heavy atoms at 10 K, followed by another 12 ps NPT minimization with restraints on solute heavy atoms and a final 24 ps NPT minimization without restraints. Following the minimization steps, the simulations were executed for 500 ns with a time step of 2.0 fs under a pressure of 1.01325 bar within an NPT ensemble framework. These molecular dynamics studies were then run using DESMOND, which

generated.out-cms files and trajectory files required for analysis.

Upon completion of the simulations, we analyzed the radial distribution functions using the Radial Distribution Function panel, in which the grouping was set to the center of mass and the SMILES codes of amide, carboxyl and hydroxyl groups were used to identify the groups. Additionally, the.out-cms file generated for each replica was subsequently imported into Maestro, where the plot function was utilized to generate graphs depicting root mean square deviation (RMSD), radius of gyration (rGyr), solvent-accessible surface area (SASA), and molecular surface area (MolSA). The.out-cms files were also imported into the Materials Science suite, for determining the interactions formed within the assemblies. The results were then exported as text files.

Protein Processing

The PDB files of the triple helix region of Type II collagen (PDB ID: 6JEC)[43] and (PDB ID: 2CUI)[44] (31st fibronectin type III domain of the human tenascin X were selected and downloaded from the RCSB Protein data bank. Any preexisting ligands structures on the proteins, and water molecules, were removed in PyMOL (2.5.2) and the protein structures were exported as .pdb files.

Molecular Docking Studies

The binding affinities of the designed peptides and peptide bolaamphiphiles with triple helix region of collagen and the fibronectin type III domain (FN III) of the human tenascin-X were determined using Autodock Vina v. 1.2.0. The clean .pdb files of the specific protein were uploaded to Autodock Tools (1.5.6.).[45,46] As before, water molecules were removed from the structure and both polar hydrogens and Kolman charges were added before a .pdbqt file was generated. Similarly, a .pdb file of the ligand was uploaded to Autodock Tools (1.5.6.) to be converted to a .pdbqt file. With both the protein and ligand .pdbqt files incorporated into the same workspace, the grid dimensions of the binding complex were set to dimensions of (40 Å × 40 Å × 40 Å) for both proteins. The grid box coordinates were (2.512, 57.052, −3.546) for collagen and (−6.570, 3.445, 5.507) for the FN (III) domain of tenascin X. Exhaustiveness and energy range were kept at their default values of 8 and 4, respectively. The .pdbqt files of the protein and ligand as well as the grid dimensions were inputted into the Autodock Vina v. 1.2.0 software, which provided a ranking of the most optimal binding affinities of the binding complex as well as an output file of these potential structures.

Protein–Ligand Interaction Profiler (PLIP)

The specific binding interactions of complexes between the ligands and proteins were analyzed using the Protein–Ligand Interaction Profiler (PLIP) online interface.[47] The .pdbqt file of the Autodock output was opened in PyMOL (2.5.2) along with the clean .pdb file of the protein and exported together as a single .pdb file for the bound complexes. This .pdb file was then uploaded to the webserver, which generated a list of interactions in .txt format and a binding model in .pdb format. While the results from the .txt file were tabulated, the .pdb file generated from PLIP was opened in PyMOL (2.5.2) and the binding interactions between the protein and ligand were labeled.

Laboratory Methods

Materials

The peptide WMYGGGWMY was custom ordered from GenScript (Piscataway, NJ, USA). Juvenile normal human epidermal keratinocytes (NHEK) (C-12005), human collagen type II, N-hydroxysuccinimide (NHS), collagen (type II), 1-ethyl-3-(3-dimethylaminopropyl) carbodiimide (EDAC), dimethylformamide (DMF), Triton-X, and 1,4 butane diamine were purchased from Sigma Aldrich (St. Louis, MO, USA). Adult human dermal fibroblasts (HDF), phosphate-buffered saline (PBS), fetal bovine serum (FBS), and antibiotic-antimyotic, were ordered from ATCC (Manassas, VA, USA) for use in cell culture. Other cell culture materials, such as 0.05% Trypsin-EDTA and Corning fibroblast growth medium and supplement were purchased from Thermo Fisher Scientific (Waltham, MA, USA). The Dojindo DPPH antioxidant assay kits was purchased from Cayman Chemical Company (Ann Arbor, MI, USA). MTT cell proliferation assay kits and Phalloidin CruzFluor 488 conjugate antibody were purchased from Santa Cruz Biotechnology (Dallas, TX, USA). Formaldehyde (4%) in phosphate-buffered saline was procured from Boston Bioproducts (Ashland, MA, USA). All materials used for bioprinting were acquired by CELLINK (Boston, MA, USA), including 25 G, 250 µm sterile standard conical bioprinting nozzles and 3 mL cartridges. Tenascin-X was custom ordered from MyBioSource.

Synthesis of Peptide Bolaamphiphile WMYGGGWMY-C4-YMWGGGYMW

The peptide WMYGGGWMY was conjugated with 1,4 diamino butane in a 2:1 ratio using traditional peptide coupling methods.[48] Briefly, the peptide WMYGGGWMY (1 M) was dissolved in DMF followed by the addition of EDAC (0.5 M) and NHS (0.5 M) to

activate its terminal carboxyl group. This mixture was shaken at 4°C for 1 h at 100 rpm. Butane, 1, 4 diamine (0.5 M) was then added to the mixture and shaken at 100 rpm and 4°C for 48 h. The resulting product was dried using rotary evaporation. The product obtained was then recrystallized from acetone and dried using a SpeedVac, Vacuum Concentrator System. The chemical structure of the formed product was confirmed by ^{1}H NMR using a Bruker 400 MHZ NMR spectrometer and FTIR spectroscopy. The proton NMR spectrum obtained indicated the following peaks. δ 1.43 (4 h, m); δ 2.0 (m, 8 h); δ 2.1 (12 h, s); δ 2.72 (t, 8 h); δ 3.21 (4 h, t); δ 3.35; (8 h, d); δ 3.51 (d, 8 h); δ (3.90, 2 h); δ 4.12 (12 h, s); δ 4.31 (t, 4 h); δ 4.83 (t, 6 h); δ 6.72 (8 h, d); δ 6.92 (8 h, d); δ 7.01 (4 h, d); δ 7.16 (4 h, m); δ 7.25 (s, 4 h); δ 7.4 (4 h, d); δ 7.62 (4 h, d); δ 8.0 (2 h, s); δ 8.21 (10 h, s); δ 8.81 (4 h, s): δ 8.94 (6 h, s). δ 10.82 (s, 4 h).

Self-Assembly of WMYGGGWMY-C4-YMWGGGYMW

The synthesized product (0.1 M) was allowed to self-assemble in an aqueous solution over a period of one week at room temperature. The growth of the assemblies was followed using dynamic light scattering. The nanoassemblies were then dried and stored at 4°C for further analysis.

Formation of WMYGGGWMY-C4-YMWGGGYMW Biocomposites

The nanoassemblies (0.1 M) were reconstituted in aqueous solution followed by addition of Collagen Type II (50 μg/mL), NHS (0.05 M) and EDC (0.05 M) and shaken for 72 h at 4°C for the formation of collagen-bound nanoassemblies. The collagen-bound assemblies were then centrifuged and washed twice with deionized water and dried and analyzed. To incorporate tenascin-X, the dried collagen-bound assemblies were once again reconstituted in deionized water followed by the addition of tenascin-X (50 μg/mL) in the presence of NHS (0.05 M) and EDAC (0.05 M) were and allowed to shake for 72 h, followed by centrifugation and drying using speed-vac. The formed scaffold was then stored at 4°C for further use.

Rheological Analysis

To investigate the mechanical properties of the formed biocomposites, samples were subjected to frequency sweeps within a range of angular frequencies from 0.1–100 rad/s using a Discovery Hybrid HR2 Rheometer (TA instruments, New Castle, DE, USA). The storage (G') and loss moduli (G") as well as the complex viscosity of the samples were measured. A stainless steel peltier plate with an 8 mm peltier cone geometry was used at two different stain percentages: 1% and 5%. All measurements were triplicated and conducted in air.

Differential Scanning Calorimetry (DSC)

The thermal phase changes of the nanoassemblies as well as the biocomposite scaffolds was analyzed using differential scanning calorimetry using a TA Instruments Q200 DSC (TA Instruments, New Castle, DE, USA). For each construct, 2.5 mg of sample was dried, weighed and pressed into aluminum pans using a Tzero sample press. The samples were then loaded into the DSC and heated from 0°C to 200°C with steady nitrogen flow.

Antioxidant Assay

To examine the antioxidant abilities of the biocomposites, 1,1-diphenyl-2-picrylhydrazil (DPPH) radical scavenging assays[49] were performed. The reagents were prepared according to manufacturer's instructions. Briefly, first, a preliminary experiment using a 96-well plate was performed to determine the ideal concentration ranges for the biocomposite scaffolds. For this preliminary experiment, four 10-fold dilutions of the construct solutions were plated and water was added to control wells. Then, 80 μL of assay buffer was added to each well, followed by DPPH (100 μL) working solution to all sample wells and the blank 1. The plate was then incubated at 25°C for 30 min in the dark. Following incubation, the absorbance at 520 nm was measured using a Biotek plate reader. The optimal concentration ranges of each sample were determined as those that resulted in 50% radical scavenging. Once sample concentration ranges were determined, samples were plated in a 96-well plate for each construct. The standard solution (Trolox) was also added to the wells for which five serial dilutions were used. Assay buffer (80 μL) was then added to each well followed by DPPH (100 μL) working solution to each sample and Trolox wells. The plate was then incubated at 25°C for 30 min in the dark, and the absorbance was measured using a Biotek Eon plate reader. Measurements were taken at 520 nm in 10-min intervals over a span of 1 h to analyze if there was a change in antioxidant activity over time. The inhibition ratio was determined using the same calculations used in the preliminary experiment. The inhibition ratio of each sample at each concentration was determined by the equation inhibition ratio of sample (%) = $(A_{CS} - A_S)/A_{CS} \times 100$, where A_{CS} is the absorbance of Blank 1 - the absorbance of Blank 2 (solvent-water) and A_s is the absorbance of the sample – the absorbance of Blank 2.

Biodegradability Studies of the Scaffold

The biodegradation behavior of the biocomposite scaffold was examined in a simulated body fluid (SBF)[50]

purchased from Biochemazone at pH 7.4 and 37°C. The SBF solution was changed every 24 h by decanting the solution and replacing it with an equal amount of the SBF, and the cumulative weight loss was calculated as a function of time.

Characterization

Dynamic Light Scattering (DLS)

Dynamic light scattering analysis was performed to determine the size distribution of the assemblies over time using a Malvern Panalytical Zetasizer Ultra. In general, 10X dilutions of were utilized for measurements. Each sample was read thrice.

Fourier Transform Infrared Spectroscopy (FTIR)

FTIR spectra were measured with a ThermoFisher Scientific Nicolet iS50 FTIR (Waltham, MA, USA) from 1000 to 4000 cm^{-1}. One hundred scans were performed for each sample.

Scanning Electron Microscopy (SEM)

To determine the morphologies of the structures of the nanoassemblies as well as the biocomposites, scanning electron microscopy was performed using a Zeiss EVO MA10 model SEM. For each construct, samples were spread on carbon tapes and allowed to dry overnight. Samples were loaded into the SEM and imaged at multiple magnification levels and within the range of 5–10 kV.

Cell Studies

2D Cell Cultures

To examine cellular interactions of the biocomposite scaffolds with mammalian cells, two cell lines were investigated. Human dermal fibroblasts (ATCC PCS-201-012), were grown in fibroblast growth medium supplemented with fibroblast growth kit (containing L-glutamine: 7.5 mm, rh FGF basic: 5 ng/mL, rh Insulin: 5 µg/mL, Hydrocortisone: 1 µg/mL, Ascorbic acid: 50 µg/mL and Fetal bovine serum, 2%. Juvenile normal human epidermal keratinocytes (C-12005, Sigma Aldrich), were grown in keratinocyte growth medium with supplement mix provided. The media were also supplemented with antibiotic-antimycotic mixture (3%). Cells were grown to confluence in a 37°C incubator in a humidified atmosphere under 5% CO_2. The media was changed twice a week and cells were split as necessary. Keratinocytes and fibroblasts were then co-cultured in a 3:1 ratio for a period of 1 week before utilizing the co-cultures for bioprinting.

Cytotoxicity Studies

The cytotoxicity of the biocomposite scaffold was determined using MTT (3-(4,5-Dimethylthiazol-2-yl)-2,5-Diphenyltetrazolium Bromide) assay.[51] Keratinocytes were plated in a 96-well plate at a density of 1×10^5 cells per well and allowed to spread and adhere to the well overnight in a 37°C incubator in a humidified atmosphere under 5% CO_2. Constructs were added to the wells at three different concentrations (1 µg/mL; 2 µg/mL and 5 µg/mL) and incubated 24 h. Then, MTT reagent was prepared according to manufacturer's instructions and 10 µL of the reagent was added to each well. The cells were incubated at 37°C for 4 h. Then, the crystal dissolving solution, also prepared according to manufacturer's instructions, and then added to each well and incubated for 4 h at 37°C in 5% CO_2. A Biotek Eon plate reader was then used to measure the absorbance of the plate at 570 nm. Each study was carried out thrice, and then the results obtained were averaged. Statistical analysis was carried out using Student's t-tests.

Bioprinting

To prepare three-dimensional cell scaffold matrices using the biocomposites, droplet bioprinting was performed using a CellInk BioXTM 3D bioprinter. Droplet bioprinting was utilized due to its ability to precisely control the volume and deposition of low-viscosity cell-based bioinks and its previous applications in various forms of tissue engineering.[52] In advance of bioprinting, 3:1 co-cultures of fibroblasts and keratinocytes were grown to confluence (1×10^6 density) and transferred to a 3 mL cartridge in media. In another 3 mL cartridge, the biocomposites were loaded. These cartridges were then placed in the temperature-controlled print heads (37°C) of the bioprinter, to which 25 G, 250 µm sterile standard conical bioprinting nozzles were attached. The print bed was also set to a temperature of 37°C. Before printing, the bioprinter was manually calibrated according to the specifications of a 6-well plate. The bioprinted scaffolds were generated in a layered format. For the first layer of cells, the pressure was set to 80 kPa. The second layer, made of the scaffold, was incorporated with a pressure of 120 kPa. Changes in pressure were made as necessary to accommodate the more viscous character of the scaffolds. The extrusion for the biocomposite was repeated five times to deposit the desired amount of

the scaffold. Finally, another layer of cells was added to the scaffold with the parameters that were previously set for cell extrusion. The scaffolds were then incubated at 37°C in 5% CO_2 until further studies were performed.

Cytoskeletal Studies

To investigate the cellular interactions within the bioprinted scaffold, we conducted FITC-phalloidin cytoskeletal staining assay. Fluorescein Isothiocyanate (FITC) labeled Phalloidin is a green fluorescent stain, which binds to and labels F-actin which allows for visualization of actin within the bioprinted matrix.[53] Samples were imaged by confocal microscopy using an Agilent BioTek Cytation 10 confocal imaging reader. In general, 3-day-old and 6-day-old bioprinted scaffolds were utilized. To prepare the samples, media was removed from the wells and rinsed with PBS twice. Then, 4% formaldehyde (1 mL) in PBS was added to each well for fixing the cells for 10 min. After the formaldehyde was removed, the cell-scaffold matrices were once again rinsed with PBS twice before adding 1 mL of 0.2% triton-X. The triton-X was allowed to incubate with the cells for 4 min before being removed from the wells. Then, three drops of phalloidin were added to each sample, and the plate was incubated at 37°C for 15 min. After this incubation, samples were washed with PBS twice and then imaged by exciting samples at 488 nm.

Results and Discussion

Computational Studies

Peptide Design and Antioxidant Properties

The peptides were designed by modifying sequences obtained from natural marine resources known for their antioxidant activity and by integrating specific amino acids that are known to enhance antioxidant activity as described earlier. Among the sequences studied, the GADIVA sequence was the only peptide that was not modified, as previous laboratory studies have illustrated its strong radical scavenging activity. In general, it is well known that hydrophobic or aromatic amino acids such as Trp, Tyr, His, Leu, or Met can enhance antioxidant activity.[54] In order to predict the antioxidant activities of the newly designed peptides, we utilized AnOXPePred 1.0 webserver and compared the predicted free radical scavenging (FRS) activity scores with those of the original peptide sequences. As can be seen in Table 2, the results showed that in all cases the FRS score was higher for the designed peptides. In general, the AnOxPePred web-server utilizes a deep convolutional neural network classifier for predicting the antioxidant activity of peptides. The webserver model has been trained on a curated dataset composed of experimentally determined antioxidant and non-antioxidant peptides for predicting the free radical scavenging (FRS) and chelating properties of peptides.[29] In order to create supramolecular assemblies, the peptide bolaamphiphiles were designed. Two of the sequences (GADIVA and WMYGGWMY) were utilized to create the bolaamphiphiles ((WMYGGGWMY-CO-NH-$(CH_2)_4$-NH-CO-YMWGGGYMW (W-C4-W) and GADIVA-CO-NH-$(CH_2)_4$-NH-CO-AVIDAG (G-C4-G)). We selected these two sequences as we wanted to create bolaamphiphiles with an original known sequence (GADIVA) and WMYGGWMY which had the second highest FRS score (0.64) and contained the flexible glycine moiety as well as the aromatic tryptophan and tyrosine moieties which allow for π-π stacking interactions. In addition, there were no charged residues involved. Thus, we hypothesized that the bolaamphiphile would self-assemble efficiently through strong hydrophobic interactions as well as amide–amide hydrogen bond interactions. The two ends of butane 1,4 diamine were conjugated with the C-terminal ends of each of the peptides at both ends, thereby connecting the peptide head groups at both ends with a four-carbon alkyl chain linker through amide bonds. In the previous work, 1,4 diamino butane has been shown to aid in the formation of nanoassemblies.[55] In order to examine the ability of the peptides and the peptide bolaamphiphiles to form supramolecular assemblies, we carried out REMD simulations (Fig. 1) at three different temperatures (260 K, 310 K, and 360 K).

Table 2. Predicted free-radical scavenging activity of the designed peptides and the sequences those were derived from.

Designed sequence	Free Radical Scavenger Score	Original sequence	Free-Radical Scavenger Score
WMYGGGWMY	0.64	PMRGGGGYHY	0.59
GADIVA (same as original)	0.27	GADIVA	0.27
YYGAEFIF	0.42	GAEFIF	0.37
KYHAGAGAGHYK	0.46	PYGAKG	0.46
HMWHMWYHMW	0.68	YWDAW	0.54

Determination of Secondary Structures

In order to predict the secondary structures of the individual peptides, we utilized the webserver PSSpred. The results obtained are shown in Table 3. In general, the length of the peptides was between six amino acids (GADIVA) to twelve (KYHAGAGGHYK). Interestingly, both GADIVA and KYHAGAGGHYK were predicted to have a coiled structure, while the four other peptides were predicted to have a mix of both coiled and extended beta sheets. This is expected given that WMYGGGWMY and HMWHMWYHMW both have multiple tryptophan moieties in addition to tyrosine moieties. The YYGAEFIF sequence on the other hand, contains both multiple tyrosine and phenylalanine residues in close proximity to each other in addition to hydrophobic residues such as alanine and isoleucine and the flexible residue glycine. The presence of multiple aromatic residues is likely to promote the formation of beta-strands.[56] We also utilized AlphaFold 3 to predict the structures of the assemblies of each of the peptides. In general, we utilized 30 copies of each of the sequences to determine the predicted structures. The results are shown in Supplementary Information Figure S1. In general, the predicted Local Distance Difference Test (pLDDT) scores which estimate the extent to which the predicted structure matches with the experimental structure per-residue confidence score on a scale of 0–100 for the assemblies were compared. Overall, the values ranged from low (depicted by the yellow colorations of the structures, at 70 > pLDDT > 50) to very low (pLDDT < 50, depicted by tan color). The WMYGGGWMY, HMWHMWYHMW and KYHAGAGHYK assemblies were found to demonstrate values below 50 as indicated by the tan color of the assemblies suggestive of the presence of coils which are part of intrinsically disordered structures.[57] The GADIVA and the YYGAEFIF sequences showed assemblies in both yellow and tan colors. Given that the peptides are relatively short oligopeptides, the pTM values were below 0.5 in all cases; thus, the predicted structures may not necessarily reflect the experimental structures, as a result of the limitations of the software currently.

Molecular Dynamics Simulations

REMD Simulations for W-C4-W Bolaamphiphile. A comparison of the root mean square deviation (RMSD) plots of *W-C4-W* (Fig. 1a), shows that the largest RMSD deviations occurred at 260 K, with values ranging from approximately 1.5–3 nm before equilibrating at105 ns, and then stabilizing at 1.7 nm for the rest of the simulation. The RMSD values at the two higher temperatures demonstrate relatively lesser deviations. At 310 K, *W-C4-W* equilibrated within 20 ns, while at 360 K, *W-C4-W* equilibrated within the first 5 ns and the RMSD gradually increased to 2.05 nm by 360 ns and remained steady for the rest simulation. It is likely that at 260 K, (the lowest temperature), there may be steric clashes resulting in repulsive forces occurring initially due to proximity of molecules and the solvent, that result in a higher equilibration time.[58] When comparing the RMSD values of the three MD replicas for each of the temperatures, however, the average values of the rmsd were similar. Thus, indicating that the various replicas studies for each temperature displayed similar atomic deviations in the structure of the peptide bolaamphiphile. On average, the rmsd value across all three temperatures was found 2.03 nm and fluctuated around ~0.15 nm. The trajectory images after 105 ns of simulation corroborate with these results. In general, trajectories after 105 ns were analyzed as equilibration occurred after that time frame. As seen in Fig. 1(b), at the end of the simulation, two distinct assemblies are seen at each of the temperatures. Interestingly, at 310 K and at 260 K, one self-assembled structure is seen at 350 ns (data not shown), while for the replica at 360 K, two self-assembled structures are seen at 350 ns. Multiple structures assemblies are seen at 105 ns in all cases (data not shown).

As with the RMSD results, the rGyr values (Fig. 1c) also showed very little variation and ranged from 2.48 nm (at 360 K) to 2.88 nm (at 260 K) at the end of the simulation, particularly after the equilibration was reached. The self-assembly shows the lowest rGyr values at 360 K, with the value decreasing to 2.5 nm within the first 20 ns and remaining there for the rest of the simulation. These findings indicate that the self-assembled structures may become more compact as the temperature increases. The SASA values (Fig. 1d) show a similar trend. Overall, SASA quantitatively depicts the relationship between the assemblies and the solvent and exposed surfaces of the assemblies during molecular assembly and aggregation.[59] As the temperature increased, the SASA values are seen to be lower, indicating once again that more stable folded assemblies at 310 K and at 360 K compared to 260 K. MolSA illustrates the van der Waals surface area,[60] the probe radius was set to 1.4A° which is similar to the van der Waals surface area of water molecules. In general, values for the W-C4-W decreased with increasing temperature and after 300 ns, the average MolSA values for replicas at 360 K and at 310 K were 212 nm^2 and at 216 nm^2, respectively, while at 260 K, the average value was found to be 274 nm^2 (Supplementary Information Figure S2a) which once again indicated that relatively more stable assemblies were obtained at physiological or higher temperatures.[61] Upon investigating the interactions involved in the formation of the assemblies, as

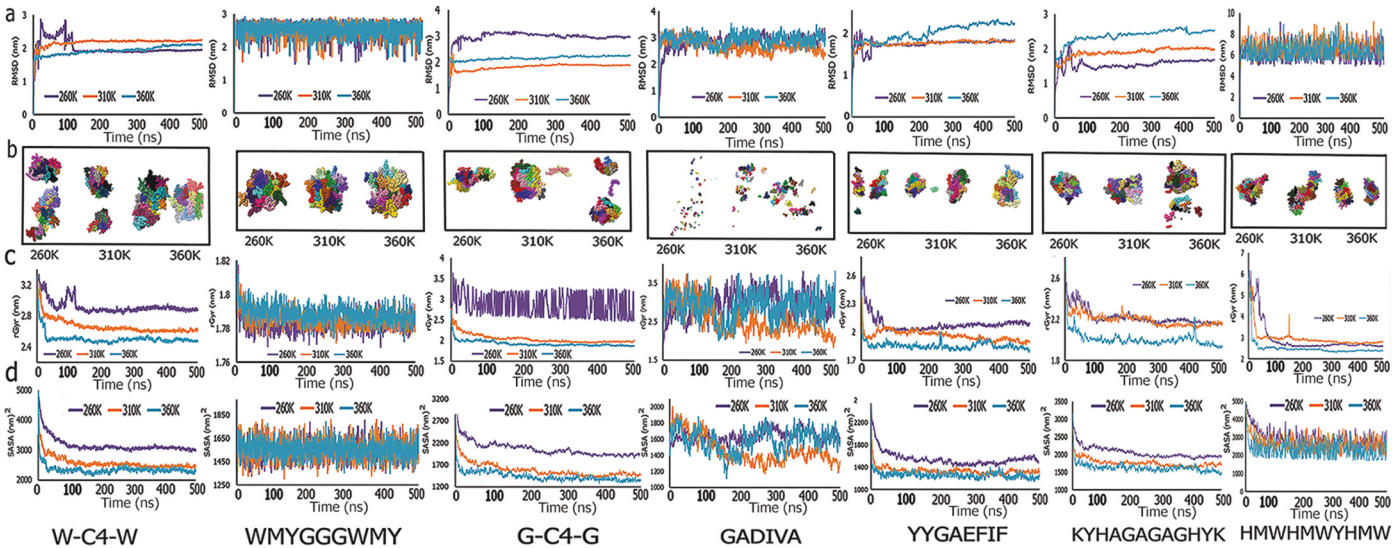

Figure 1. Row (a) RMSD values of each of the peptides and peptide bolaamphiphiles over 500 ns simulation. (b) Trajectory images of assemblies formed at the end of the 500 ns simulations at 260 K; 310 K; 360 K; (c) radius of gyration plots of each of the peptides and peptide bolaamphiphiles over 500 ns simulation at 260 K; 310 K; 360 K; (d) solvent accessible surface area (SASA) values of each of the peptides and peptide bolaamphiphiles over 500 ns simulation at 260 K; 310 K; 360 K.

Table 3. PSSpred (protein secondary structure prediction).

Peptide Sequence	Predicted Secondary Structure
WMYGGGWMY	CCCCCEEEC
GADIVA (same as original)	CCCCCC
YYGAEFIF	CCCCEEEC
KYHAGAGAGHYK	CCCCCCCCCCCC
HMWHMWYHMW	CCCCCEEECC

[C = coil; E = Extended beta-sheet].

expected π-π stacking nm^2 (Supplementary Information Figure S2b) interactions played a major role in the formation of the assemblies due to the presence of the tryptophan and tyrosine moieties, followed by hydrogen bonding interactions (Supplementary Information Figure S2c). Overall, higher interactions were observed at higher temperatures.

REMD Simulations for WMYGGGWMY Peptide

Compared to the bolaamphiphile W-C4-W, the RMSD values for neat WMYGGGWMY consistently fluctuated within the range of 1.5 nm–3 nm over the 500 ns simulation with similar trends observed for 260 K, 310 K, and 360 K indicating similar self-assembly behavior and higher convergence during the simulations across all three temperatures. The trajectory image obtained at the end of the simulation WMYGGGWMY confirm this. For all three temperatures, the peptides remained assembled into singular spherical assemblies and remain consistent throughout the simulation. The location of individual peptides within the assemblies does seem to change slightly over the course of the simulation, which might contribute to the range of values seen in the RMSD values, but they generally maintain interactions throughout the simulations.

Interestingly, the rGyr plot for WMYGGGWMY illustrates a sharp decrease from 2.28 nm to 1.78 nm within the first 5 ns of the simulation at all three temperatures. This value is notably lower than any of the rGyr values observed for W-C4-W bolaamphiphile while also being more consistent at all three temperatures. This further confirms that the WMYGGGWMY maintains a stable assembly throughout the simulation. The SASA values of WMYGGGWMY range from approximately 1400 nm^2 to 1800 nm^2 over the 500 ns simulation. Furthermore, the lower SASA values compared to W-C4-W further support that the WMYGGGWMY assemblies may be more compact and less exposed to the aqueous solvent environment.

The MolSA values ranged from approximately 1100–1500 nm^2 throughout the simulations. As seen earlier, there is a similarity in the trends observed for all temperatures. Additionally, the determined MolSA values were significantly lower for the peptide compared to the bolaamphiphile. This is expected, given that the bolaamphiphile has a larger structure and the peptide moieties are spaced apart by a hydrophobic alkyl linker. Based on the REMD data suggests that WMYGGGWMY self-assembles into compact spherical structures. Additionally, once again both π-π interactions and hydrogen bonds were involved in promoting assembly formation. However, the number of interactions were lower than those seen for the bolaamphiphile.

REMD Simulations for GADIVA-$(CH_2)_4$-AVIDAG (G-C4-G)

With respect to temperature changes, G-C4-G demonstrates similar trends as seen with the bolaamphiphile W-C4-W. The G-C4-G shows the largest RMSD values at 260 K, and demonstrated higher degree of fluctuations throughout the simulation. In comparison, at 310 K the G-C4-G equilibrated within the first 20 s to a value under 1.8 nm. The RMSD values remained steady at 360 K, stabilizing at 1.92 nm for the entirety of the simulation. The trajectory images for the G-C4-G assemblies show structural similarities to the W-C4-W self-assemblies in relation to temperature. For instance, as with the W-C4-W self-assemblies, the G-C4-G forms more elongated, fibrillar clusters at 260 K. At 310 K, the assemblies take on a more globular shape by the end of the simulation. At 360 K, varying shapes including fibrillar and globular assemblies are seen by the end of the simulation. As expected, the rGyr values for G-C4-G at 260 K fluctuated significantly during the entire 500 ns simulation between 3.5 and 2.5 nm. In contrast, the rGyr values for 310 K and 360 K were more consistent during the simulation. At 310 K, by 100 ns, the rGyr remained stable at 2 nm. Likewise, at 360 K rGyr dropped from 2.75 nm, within 25 ns, to 1.8 nm and remained steady for the rest of the simulation indicating the formation of compact clusters. The plots for SASA and MolSA of G-C4-G appear similar to those of W-C4-W in that the values decrease with increasing temperature. However, the values are generally lower for G-C4-G. The SASA values for 260 K replica begin with a maximum of around 3050 nm^2 before sharply decreasing at the beginning of the simulation. The values continue to decrease gradually until just after 300 ns, at which point the values stabilize around 2100 nm^2. For 310 K, the bolaamphiphile has an initial SASA value of around 3100 nm^2 that decreases until 300 ns to a value of 1600 nm^2 and remains stable. At 360 K, the SASA values show a similar trend and remains at 1350 nm^2 over the last 50 ns of the simulation. These results indicate that over the course of the simulation the bolaamphiphile folds up into assemblies with less areas exposed to water. Clustering analysis of the G-C4-G assemblies (data not shown) also revealed a larger

number of clusters at higher temperatures 310 K and 360 K at 16 and 17 clusters over the course of the entire simulation, while at 260 K, 10 clusters were formed. At all three temperatures, there is a decrease in the SASA within the first 300 ns indicating that the structures fold up and form assemblies within the first 300 ns. The higher SASA value at 260 K denotes the formation of relatively diffuse assemblies, while lower SASA values at 310 K and at 360 K represent the formation of more compact structures, which is also corroborated by the radius of gyration results discussed earlier.[62]

The MolSA value for G-C4-G at 260 K initially is seen at 2200 nm^2 and almost immediately drops to 1900 nm^2 before more gradually decreasing to around 1750^2 nm by the end of the simulation. At 310 K, the MolSA values decrease to 1250 nm^2 within the first 380 ns before gradually increasing to around 1400 nm^2 during the remainder of the simulation. At 360 K, the MolSA values show a similar trend before stabilizing at 1200 nm^2 by the end of the simulation. As with the SASA values, the MolSA values for G-C4-G are generally lower in value than for W-C4-W, indicating that the formed assemblies are less exposed to the solvent.

REMD Simulations for GADIVA

The RMSD values for GADIVA are generally consistent across the three temperatures. While the values for all temperatures rise at the beginning of the simulation, the values stabilize at 2.4 nm throughout the entire simulation after 20 ns. It should be noted that while the trends in RMSD generally remain consistent, the fluctuations in value throughout the simulation are greater for the peptide GADIVA than for the corresponding G-C4-G bolaamphiphile. The trajectory images for GADIVA at all three temperatures, however, indicates that a number of clusters of different shapes and sizes were formed, at all three temperatures and as a whole GADIVA peptide by itself did not self-assemble into larger assemblies. The exception being 360 K, where it appears that relatively larger and fewer assemblies are formed. These results indicate that the bolaamphiphile G-C4-G forms more stable assemblies in comparison with GADIVA. As expected, the radius of gyration also shows fluctuations in value from 2 to 4 nm over the 500 ns simulation for all three temperatures. However, the trends among the temperature variations show notable differences. While the assemblies at 260 K and 360 K both have initial rGyr values of 1.8 nm and then fluctuate before reaching an average value of 3 nm by 500 ns, at 310 K it has an average rGyr value of 3 nm during the first 150 ns before decreasing to an average of 2.5 nm for the rest of the simulation. This indicates that the assemblies are relatively more compact at 310 K (physiological temperature). Additionally, GADIVA has significantly greater and less steady rGyr values than WMYGGGWMY, suggesting that WMYGGGWMY has better potential for self-assembly compared to GADIVA.

The SASA values for the GADIVA peptide assemblies remained the most consistent at 260 K, with values averaging at about 1650 nm^2 across the entirety of the simulation. This value is significantly lower than that seen for the corresponding bolaamphiphile at 260 K. At 310 K, there was a dramatic decrease in the SASA value of GADIVA, with values decreasing to 1338 nm^2 after 250 ns and remaining within 1200–1400 nm^2 after that. This indicates that at 310 K, the GADIVA peptides are initially exposed to the solvent but over time, fold up resulting in the formation of assemblies with structures less exposed to the solvent. The MolSA values for GADIVA show similar trends with respect to time and temperature. At 260 K an average value of about 1150 nm^2 is seen, however at 310 K, the MolSA value begins decreases to an average of 950 nm^2 for the final 250 ns of the simulation. Interestingly, these values are significantly lower than those seen for the corresponding amphiphile at the same temperature, likely due to the smaller size of the peptide sequence. At 360 K the values showed the most fluctuations, with values in the range of 900–1250 nm^2.

While the SASA and MolSA values for GADIVA show more similarities with respect to thermal changes compared to G-C4-G, the values are notably different numerically for the interactions. As expected the number of hydrogen bonds was found to be significantly lower (40 to 100) for the peptide compared to that seen for the bolaamphiphile. Interestingly, the peptide also showed the formation of salt-bridges which were not observed in the case of the bolaamphiphile. As anticipated no π-π stacking interactions were observed GADIVA or G-C4-G due to the absence of aromatic groups.

We also carried out REMD simulations of three of the individual additional antioxidant peptides YYGAEFIF; KYHAGAGAGHYK and HMWHMWYHMW. As can be seen, the RMSD values indicate that of the three peptides, the most consistent RMSD values across all three temperatures are seen for the peptide HMWHMWYHMW. Furthermore, the values were significantly higher (6–8 nm) for this peptide compared to all other peptides. In the case of YYGAEFIF and KYHAGAGAGHYK, the RMSD values ranged from 1.5 nm to 2.4 nm and faster equilibration was seen at higher temperatures in both cases while at 260 K, equilibration was achieved after 100 ns. In general, by the end of the simulation, multiple fibrous structures are seen for

the HMWHMWYHMW peptide at all temperatures. The KYHAGAGAGHYK peptide on the other hand, self-assembles into multiple fibrous and spherical structures by the end of the simulation at 360 K, and single spherical compact assemblies at lower temperatures. The YYGAEFIF peptide forms multiple fibrous and oblong-shaped assemblies across all three temperatures. The radius of gyration values shows a similar trend for all three peptides, in that all of the peptides show a dramatic decrease in the radius of gyration values within the first 50 ns and remain stable for the rest of the simulation. For the YYGAEFIF and KYHAGAGAGHYK peptides the values stabilize between 1.9 and 2.1 nm across all three temperatures. Interestingly, while the rGyR values start at 6 nm for the HMWHMWYHMW peptide, after 150 ns, each of these stabilize between 2.3 nm and 2.7 nm indicating that over time more compact structures are formed in all cases. Among the three peptides the highest SASA values are seen for the HMWHMWYHMW peptide as expected due to the presence of polar, charged residue histidine[63] which may interact more favorably with the solvent (water). A similar trend was seen at all temperatures, where the SASA values remained consistent between 2000 nm^2 and 3000 nm^2 across all temperatures for this particular peptide. The lowest SASA values were seen for the YYGAEFIF peptide where the values ranged from 1213 nm^2 to 1479 nm^2, while for the KYHAGAGAGHYK peptides, the SASA values were found to be in the intermediate range between 1484 nm^2 to 1954 nm^2. The lowest SASA values for the YYGAEFIF peptide can be attributed to the presence of mostly hydrophobic residues, with the exception of the glutamic acid moiety, while the KYHAGAGAGHYK peptide showed contained charged residues such as lysine and histidine, which could interact with the solvent. A similar trend was observed for the MolSA values, where the values decreased after 100 ns, and remained consistent for the rest of the simulation. The lowest MolSA values were seen for the YYGAEFIF peptide, while the highest was seen for the HMWHMWYHMW peptide. As expected, all three peptides demonstrated that the assemblies were promoted through both hydrogen bond interactions and π-π stacking interactions, with π-π stacking interactions being the highest for the HMWHMWYHMW peptide. Overall, these results indicate that while all of the peptides could form self-assembled structures. The WMYGGGWMY peptide and its bolaamphiphile as well as the GADIVA bolaamphiphile also may be predicted to form stable supramolecular assemblies.

We also investigated the radial distribution functions $g(r)$ (RDF) between different pair structures around the center mass of the amide groups, carboxyl and hydroxyl groups to further explore the self-assembly process and formation of clusters (Fig. 2). As seen in Fig. 2(a), interestingly the highest RDF values were seen for the W-C4-W bolaamphiphile, for the amide group at all three temperatures. Additionally, the two relatively sharp peaks were observed, illustrating the strong involvement of the amide groups in self-assembly of this bolaamphiphile. The hydroxyl group interactions also showed a strong sharp peak followed by a relatively short broad peak, indicating the involvement of hydroxyl groups in cluster formation, though to a lesser extent compared to the amide group. Comparatively the G-C4-G bolaamphiphile (Fig. 2c), showed relatively broad RDF peaks, indicating relatively disordered structure formation across all three temperatures. While the amide and carboxyl contributions were similar, the hydroxyl group interaction was higher.

Among the peptides, for the WMYGGGWMY peptide (Fig. 2b), the carboxyl interactions showed a strong narrow peak at 260 K, indicative of its contribution to the formation of the assemblies at that temperature, while hydroxyl groups were found to contributeat 360 K which indicates its contribution to clustering[64] at the higher temperature. The amide RDFs were found to show multiple broad peaks at higher distances, indicative of their weaker contribution and the formation of relatively disordered structures.[65] H-bonding between the carboxyl groups as well as between the amide groups is largely responsible for cluster formation. Interestingly, the GADIVA peptide (Fig. 2d) did not show hydroxyl group interaction, indicating that those interactions were not specifically involved in cluster formation. This is expected due to the absence of hydroxyl groups within the peptide sequence. The amide group interactions, however, showed prominent peaks at 310 K indicating its involvement in cluster formation. Relatively shorter and broad peaks were observed at 360 K and at 310 K indicating the formation of relatively disordered structures. The YYGAEFIF peptide (Fig. 2e) also showed a prominent broad peak (between 2 A° and 4.5 A°) at 260 K and between 3 A° and 4.5 A° for the carboxyl group, indicating these interactions were involved in cluster formation, while at 360 K, broad interactions were seen resulting in relatively less ordered structures. The amide groups showed relatively strong peaks at 310 K, but at higher "r" values indicating their contributions through relatively weaker interactions. The RDF for the hydroxyl group showed a sharp, narrow peak at a shorter distance (between 0.3 A° and 0.6 A°) followed by shorter peaks at 310 K, indicating their strong contribution to cluster formation due to the hydroxyl group interactions between the tyrosine moieties. A similar trend was observed for the

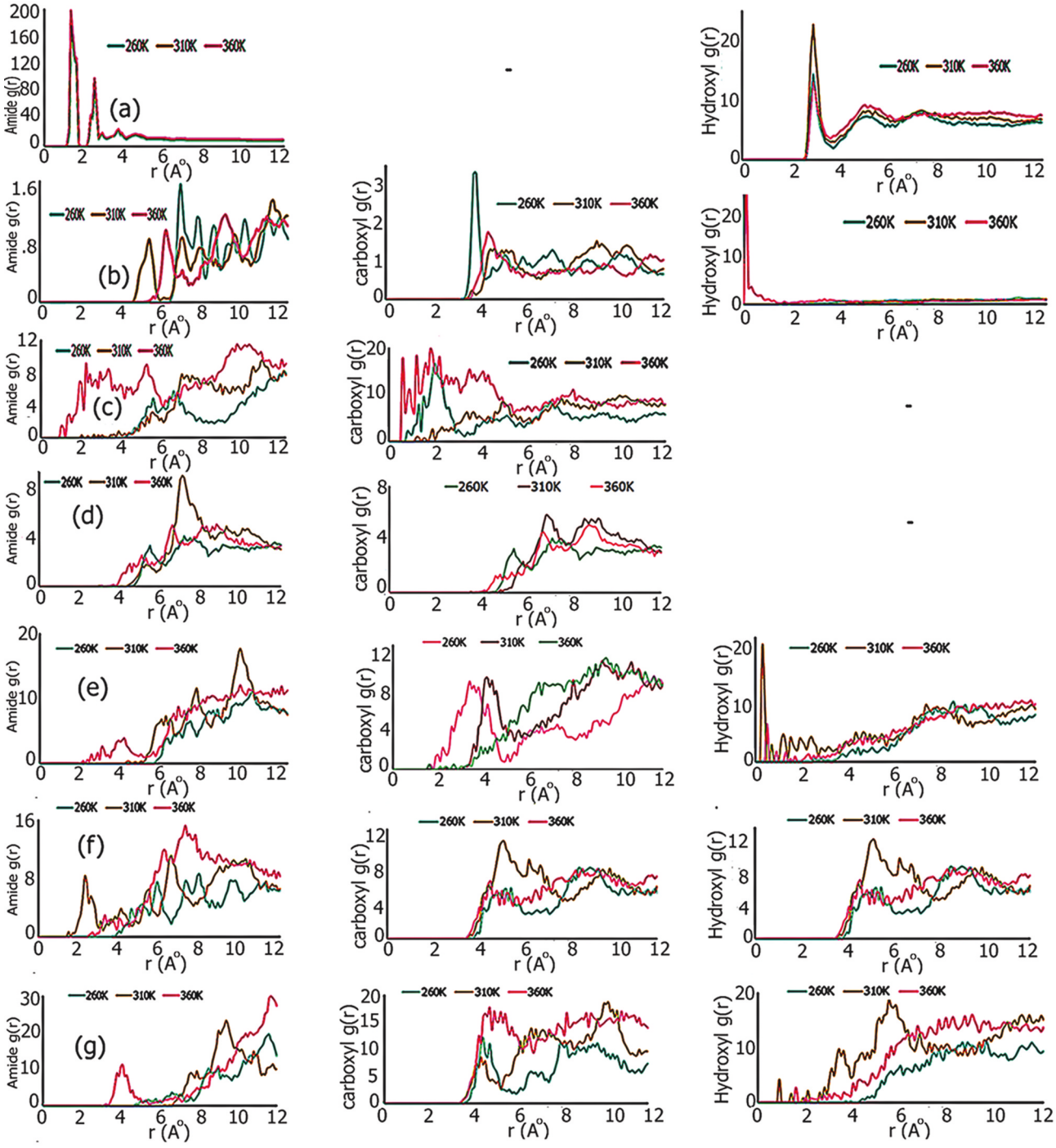

Figure 2. Radial distribution functions obtained from the 500 ns trajectories for the REMD simulations at three different temperatures. From left to right, the interactions between –NH–O = C–(amide), –COOH—HOOC (carboxyl), and –OH—HO– (hydroxyl group) interactions were investigated for the bolaamphiphiles and peptide sequences. (a) W-C4-w; (b) WMYGGGWMY; (c) G-C4-G; (d) GADIVA; (e) YYGAEFIF; (f) KYHAGAGAGHYK; (g) HMWHMWYHMW.

KYHAGAGAGHYK peptide (Fig. 2f) with a sharp strong peak observed for the hydroxyl group, at "r" values between 0.2 A° and 0.4 A° at 310 K, followed by broad peaks. Additionally, the highest RDF for the carboxyl interaction was also seen at 310 K. A relatively narrower peak was also observed between 1.7 A° and 2.5 A° for the amide interaction at 310 K, followed by additional peaks at higher *r* values likely due to formation of multiple layers of assemblies. The highest RDF for the amide interaction was observed at 360 K, though at a larger *r* value, indicative of weaker contribution to cluster formation. Intermediate results were observed at

260 K. The HMWHMWYHMW peptide (Fig. 2g) showed broader RDF peaks overall. While at 360 K, the amide group interaction showed a relatively strong peak between 3 A° and 6 A°, the carboxyl group interaction peak was seen between 4 A°and 6 A° at all three temperatures followed by broad peaks due to weak interactions. The hydroxyl group interaction on the other hand appears to play a more prominent role at 310 K compared to that at the other two temperatures. Overall, the REMD simulations indicate that the peptide bolaamphiphiles, particularly W-C4-W, showed strongest interactions through amide groups, and hydroxyl groups while the weakest interactions were observed for the neat peptide GADIVA. All other constructs showed relatively intermediate interactions and resulted in the formation of globular or fibrous supramolecular assemblies.

Binding Interactions with Extracellular Matrix Proteins

To develop a biocompatible scaffold, it is imperative that the formed supramolecular assemblies can interact favorably with the ECM proteins.[66] Thus, upon confirmation that the peptides and the bolaamphiphiles were capable of self-assembly, we then conducted molecular docking studies to examine their binding affinities toward extracellular matrix proteins (ECM). Specifically, the peptides were docked with fibronectin type III domain of tenasicin X, and the triple helix domain region of collagen type II as these proteins form an integral part of the ECM. The results obtained are shown in Table 4. As can be seen, the sequence WMYGGGWMY displayed the highest binding affinity toward the fibronectin type III domain of tenascin X. Interestingly, both WMYGGGWMY and W-C4-W bolaamphiphile demonstrated similar binding affinities with the triple-helix domain region of collagen. The peptide YYGAEFIF showed the highest binding with the triple helix region of collagen. However, peptides GADIVA and KYHAGAGAGHYK showed the lowest binding affinities with tenascin-X fibronectin type III binding region, while the peptide HMWHMWYHMW demonstrated intermediate binding affinity.

Protein–Ligand Interactions Profiler (PLIP)

To shed light on the binding interactions involved between the ECM proteins and the peptides and peptide bolaamphiphiles, we conducted PLIP analysis. Results are shown in Supplementary Information Table S1 and Figures 3 and 4. We specifically chose the FN (III) region of Tenascin-X due to its regulatory impact on cell adhesion and migration as well as its ability to bind to vascular endothelial growth factor (VEGF).[67] As can be seen, in the case of the FN (III) domain of Tenascin X, the peptide bolaamphiphile W-C4-W (Fig. 3a) displayed the highest number of hydrogen bond interactions (14), while the neat peptide WMYGGGWMY (Fig. 3b) showed ten hydrogen bonding interactions. Interestingly, the neat WMYGGGWMY peptide displayed six hydrophobic interactions while the corresponding bolaamphiphile displayed five hydrophobic interactions. Moreover, while both the bolaamphiphile and the neat peptide formed three hydrogen bonds with SER47, the bolaamphiphile also showed several interactions with residues including GLN100, ILE99 and THR86, and LEU12 and LEU15. On the other hand, the peptide primarily interacted with residues such as PRO46, HIS54, GLU52, ARG56, and SER84 and LEU82 which lie within the central region of the 31st FN (III) domain. This indicates that the bolaamphiphile due to its larger size and flexibility of the linker may form a more extended structure with tenasicin-X fibronectin type III domain. Interestingly, the G-C4-G bolaamphiphile (Fig. 3c) also showed interactions with HIS54, ARG56 and Ser84 which were common with the WMYGGGWMY peptide, but in addition, it also interacted with ARG42 which was seen for W-C4-W. No interactions were seen with THR102 or LEU12 indicating that this particular bolaamphiphile displayed a relatively less extended structure compared to W-C4-W due to its smaller size. Another notable point was that GADIVA (Fig. 3d) and its corresponding bolaamphiphile formed salt bridges with ARG56 and ARG42, respectively. Furthermore, while GADIVA formed three hydrogen bonds with TYR88, and one hydrogen bond each with LYS95 and THR86, its corresponding bolaamphiphile formed two hydrogen bonds each with residues such as SER84, THR86, and LEU59, while both

Table 4. Molecular docking studies showing binding affinities.

Compound	FN (III) domain of Tenascin X (kcal/mol)	Triple-Helix region of Collagen II (kcal/mol)
W-C4-W	−5.5	−4.8
WMYGGGWMY	−7.0	−4.8
G-C4-G	−6.0	−4.4
GADIVA	−4.8	−4.9
YYGAEFIF	−6.0	−5.0
KYHAGAGAGHYK	−4.4	−4.0
HMWHMWYHMW	−5.1	−4.1

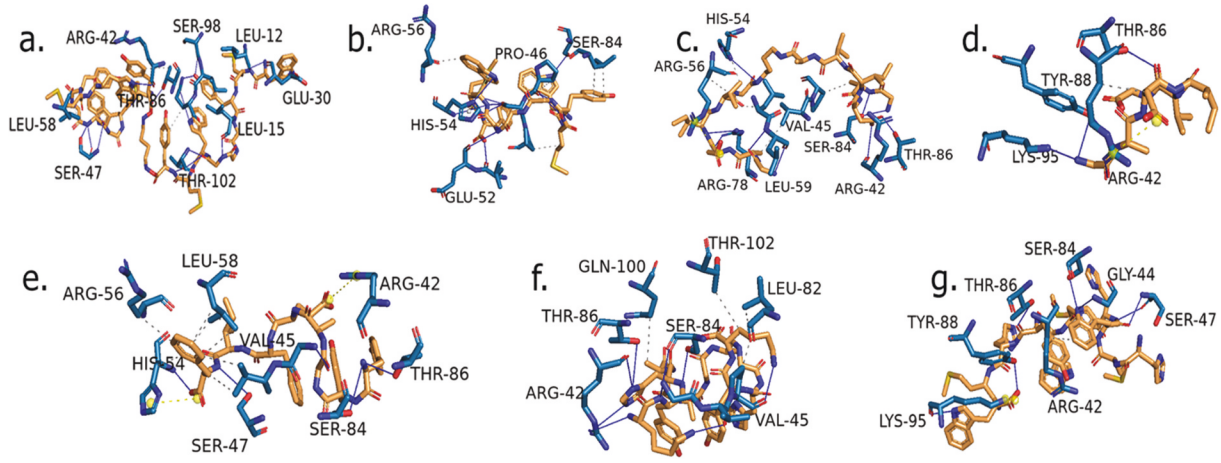

Figure 3. PLIP results obtained for each ligand upon binding with FN (III) binding domain of Tenascin. (a) W-C4-w; (b) WMYGGGWMY; (c) G-C4-G; (d) GADIVA; (e) YYGAEFIF; (f) KYHAGAGAGHYK; (g) HMWHMWYHMW. Black dotted lines are indicative of hydrophobic interactions while blue sold lines indicate hydrogen bonds. Yellow dotted lines show salt bridges.

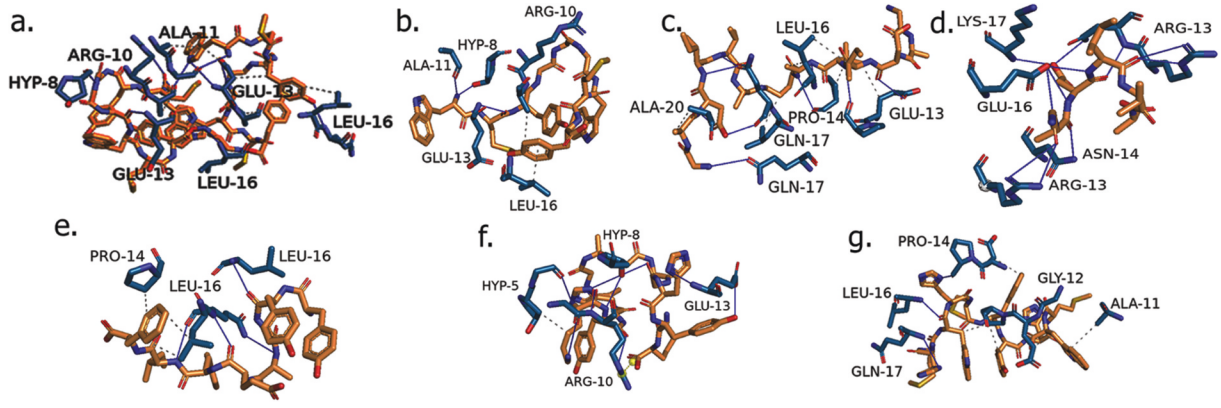

Figure 4. PLIP results obtained for each ligand upon binding with triple-helix region of type II collagen. (a) W-C4-w; (b) WMYGGGWMY; (c) G-C4-G; (d) GADIVA; (e) YYGAEFIF; (f) KYHAGAGAGHYK; (g) HMWHMWYHMW. Black dotted lines are indicative of hydrophobic interactions while blue sold lines indicate hydrogen bonds.

GADIVA peptide and its bolaamphiphile formed hydrogen bonds with ARG42. In fact, ARG42 was found to interact with all of the peptides including KYHAGAGAGHYK, HMWHMWYHMW and YYGAEFIF (Figs. 3e–3g) either through salt bridge, hydrogen bond or hydrophobic interaction with the exception of WMYGGGWMY. Other common interactions seen for the peptides KYHAGAGAGHYK, HMWHMWYHMW, and YYGAEFIF included hydrogen bonds with SER84, THR86, and GLY44. Notably, the YYGAEFIF sequence was the only peptide to form two salt bridges with both ARG42 and HIS54, and also showed the highest number of hydrophobic interactions (eight) among all the peptides. Additionally, the lowest number of hydrophobic interactions was seen for HMWHMWYHMW (one), while KYHAGAGAGHYK was the only peptide to show interactions with residues such as GLN100 and THR102, similar to the W-C4-W bolaamphiphile.

Protein–Ligand Interactions Profiler (PLIP) with Triple Helix Domain of Collagen

We also examined the binding interactions of each of the peptides and both the peptide bolaamphiphiles with the triple helix domain of Type II collagen (Figs. 4a–4g). Similar to tenascin-X fibronectin type III domain, the peptide bolaamphiphile W-C4-W also showed the highest number of hydrogen bond interactions (10) with the triple helix region of collagen. Additionally, the peptide KYHAGAGAGHYK also showed 10 hydrogen bond interactions. The W-C4-W bolaamphiphile showed the highest number of hydrophobic interactions at seven, while KYHAGAGAGHYK only showed one hydrophobic interaction. Interestingly, a common interaction seen for all the

bolaamphiphiles and the peptides was with the charged residue GLU13 with the exception of the YYGAEFIF peptide. Furthermore, GLU13 showed the highest number of interactions with the W-C4-W bolaamphiphile, (two hydrophobic and three hydrogen bond interactions). In previous work, the glutamic acid residue of collagen II has also been shown to aid in the formation of stable chitosan-collagen II complexes and therefore this particular interaction is promising.[68] Interestingly, KYHAGAGAGHYK formed four hydrogen bonds with HYP8 and one hydrophobic interaction with HYP5, while WMYGGGWMY and its bolaamphiphile (W-C4-W) formed one hydrogen bond each with HYP8 and GADIVA formed one hydrophobic interaction with HYP8. No other peptides or bolaamphiphiles interacted with hydroxyproline residues. Notably, while ALA11 was involved in two hydrophobic interactions as well as two hydrogen bonds with the W-C4-W bolaamphiphile, it only formed one hydrogen bond with the peptide WMYGGGWMY, and one hydrophobic interaction each with GADIVA and the HMWHMWYHMW peptide. The G-C4-G bolaamphiphile showed interactions with ALA20 instead. Other prominent interactions seen for the G-C4-G bolaamphiphile were with GLN17 with which it formed four hydrogen bonds; PRO14 (2 hydrogen bonds and one hydrophobic interaction) and with LEU16 (three hydrophobic interactions). In comparison, the neat peptide GADIVA did not show any of those interactions; instead, it formed five hydrogen bonds with the charged residue ARG10. This implies that binding interactions varied significantly between GADIVA and its G-C4-G bolaamphiphile. The GLN17 residue also played a prominent role in interacting with the YYGAEFIF peptide with which it formed three hydrogen bonds and with HMWHMWYHMW with which it formed one hydrogen bond. Among the glycine residues of Type II collagen, GLY12 formed one hydrogen bond each with the W-C-W bolaamphiphile and the HMWHMWYHMW peptide; one hydrogen bond was seen with GLY9 and with GLY6 for the KYHAGAGAGHYK peptide and one hydrogen bond was formed between the GADIVA peptide and GLY9.

As with tenascin-X Fn (III domain), hydrogen bonds showed consistently high interactions with most of the peptides and the bolaamphiphiles, the only exception being the HMWHMWYHMW peptide which displayed five hydrophobic interactions and only four hydrogen bonds. Overall, charged residues such as GLU13, ARG10 appeared to be involved in hydrogen bond interactions with most of the peptides or bolaamphiphiles, while ALA11, LEU16 and PRO14 were seen in many of the hydrophobic interactions. One unique interaction seen only for the G-C4-G bolaamphiphile was with ALA20. These results confirm that the peptides and the bolaamphiphiles interact favorably with triple helix region of Type II collagen.

Experimental Studies

Growth of W-C4-W Assemblies and Formation of Scaffold

Given the overall computational results, as a proof of concept, we the synthesized the W-C4-W bolaamphiphile and examined the growth of supramolecular assemblies. The growth of the assemblies was examined by dynamic light scattering analysis over time. As can be seen in Supplementary Information Figure S4, over time, we observed an increase in the sizes of the assemblies as demonstrated by the size distribution of assemblies formed after 72 h, 120 h and 192 h. As can be seen by 192 h, a bimodal distribution is observed and the average size of the assemblies were found to be between 1039 nm and 1209 nm in diameter.

The formation of the assemblies was also confirmed by SEM analysis (Fig. 5). As can be seen multi-layered fibrous petal-shaped nanoassemblies (Fig. 5a) are observed after 1 week of growth of the peptide bolaamphiphile. The growth can be attributed to stacking interactions between the tryptophan and tyrosine moieties as well as hydrogen bond interactions between the amide groups of the peptide moieties. Additionally, the butyl linker, tyrosine, and tryptophan moieties may also contribute to hydrophobic interactions. In previous work, it has been shown that peptide amphiphiles or hybrid peptide-nucleic acids containing aromatic moieties such as phenylalanine or tryptophan can self-assemble into nanofibers.[69] Because tryptophan contains the indole ring system, it is not only capable of stacking interactions, but the NH-group of the indole ring can also participate in hydrogen bonds.[70] In addition, π-cation interactions are also known to occur. Furthermore, the presence of multiple glycine moieties promote backbone hydrogen bonding, while the hydrophobic $(-CH_2)_4$ linker allows for intermolecular hydrophobic interactions, further promoting the formation of the assemblies.

When collagen was incorporated, (Fig. 5b) we observed the formation of fibrous hierarchical assemblies. In general, it is well known that the triple helix structure of collagen promotes the formation of fibrillar assemblies that can mimic the extracellular matrix and allow for the formation of nano and microscale biocompatible scaffolds.[71] The binding between the W-C4-W assemblies and collagen was promoted by interactions

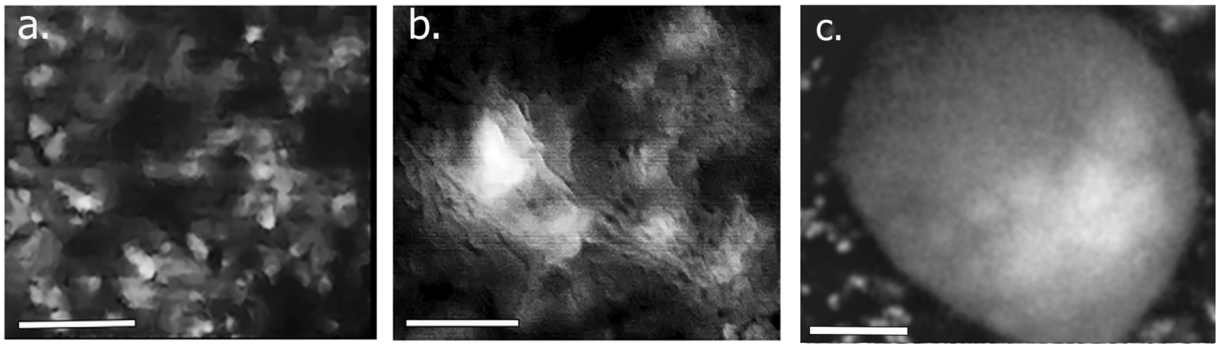

Figure 5. SEM images of (a) W-C4-W nanoassemblies; (b) W-C4-W nanoassemblies bound to collagen; (c) W-C4-W nanoassemblies bound to collagen and tenascin-X. (a) and (c) scale bar = 2 μm; (b) scale bar = 1 μm.

between backbone glycine hydrogen bonds of collagen and that of the peptide moieties of W-C4-W in addition to hydrophobic interactions. Upon binding with tenascin-X, we observed the formation of a mesh of gelatinous structure (Fig. 5c). Tenascin-X is a glycoprotein containing N-terminal EGF-like repeats,[72] as well as several fibronectin-III repeats, and a C-terminal fibrinogen-like domain which can aid in the formation of the gelatinous matrix, and thereby not only interact with cells but also in mimic the extracellular matrix. These results further confirm the formation of the biocomposiste scaffold.

FTIR Spectroscopy

To confirm the formation of the scaffolds, we conducted FTIR spectroscopy. Figure 6 shows a comparison of the FTIR spectra of the self-assembled peptide W-C4-W bolaamphiphile and those of the formed scaffolds. As can be seen, the neat assemblies showed distinct peaks at 1726 cm^{-1}, and at 1680 cm^{-1} as well as a short peak at 1631 cm^{-1} in the amide I region while the amide II peak was seen at 1521 cm^{-1}. The -CH_2- in plane scissoring vibration peak is seen at 1481 cm^{-1}, while the peaks at 1399 cm^{-1} and 1370 cm^{-1} are attributed to –CH_2 bending and –CH_3 bending vibrations respectively.[73] The C-O stretching peaks are seen at 1254 cm^{-1} and at 1023 cm^{-1}. In contrast, upon incorporation of collagen with the peptide bolaamphiphile assemblies, a broad carbonyl peak was observed at 1655 cm^{-1} in the amide I region, while the amide II peaks are seen at 1551 cm^{-1} and 1521 cm^{-1}. The appearance of these peaks upon binding with the nanoassemblies confirm the incorporation of type II collagen.[74] Upon incorporation of tenascin-X, a glycoprotein, the amide I peak shifted to 1643 cm^{-1}, while the amide II bands were seen at 1555 cm^{-1} and at 1517 cm^{-1}. Furthermore, the C–O peak was shifted to 1219 cm^{-1} compared to that seen for the collagen-bound scaffold at 1207 cm^{-1}. The C-O peak was also shifted to 1113 cm^{-1}.[75]

DSC Analysis of Scaffolds

In order to further assess the thermal phase changes of the formed scaffold, we performed DSC analysis (Fig. 7). As can be seen for the self-assembled W-C4-W assemblies, we observed two short broad endothermic peaks at 60°C and at 89.2°C due to changes in hydrogen bond interactions and unfolding of the assemblies as well as gradual loss of residual water.[76] As described earlier, the formation of the assemblies was promoted by strong non-covalent interactions such as hydrogen bond interactions and stacking interactions between the peptide moieties. As the assemblies are heated, those hydrogen bonds tend to reorganize, which leads to unfolding of the nanoassemblies. A broad endothermic peak is also observed at 161°C likely due to thermal melting of the nanoassemblies. Upon incorporation of collagen, while the short broad endothermic were found to be at slightly lower temperatures (58.8°C and 87.5°C, respectively), which is expected due to the integration with collagen, there was a significant decrease in the thermal melting temperature to 148.1°C in addition to the appearance of a short endothermic peak at 126°C. Furthermore, a new thermal transition, at 176°C was observed. The changes observed compared to the nanoassemblies can be attributed to the formation of collagen-blended nanoassemblies. In previous work, it has been shown that unfolding of collagen due to breaking of hydrogen bonds that form the hydration network around the collagen molecules occurs around 58°C–68°C,[77] while the thermal transitions seen at around 150°C may be due to gelatinization of the collagen fibrils and degradation. Interestingly, upon incorporation of tenascin-x, the first endothermic peak was seen between 50.1°C and 82.1°C, though its appearance was significantly less prominent and broad compared to the nanoassemblies or those seen for collagen-bound assemblies. These changes can be attributed to cross-linking of collagen and tenascin-X with the assemblies. The endothermic peaks are seen at higher temperature (152°C and at

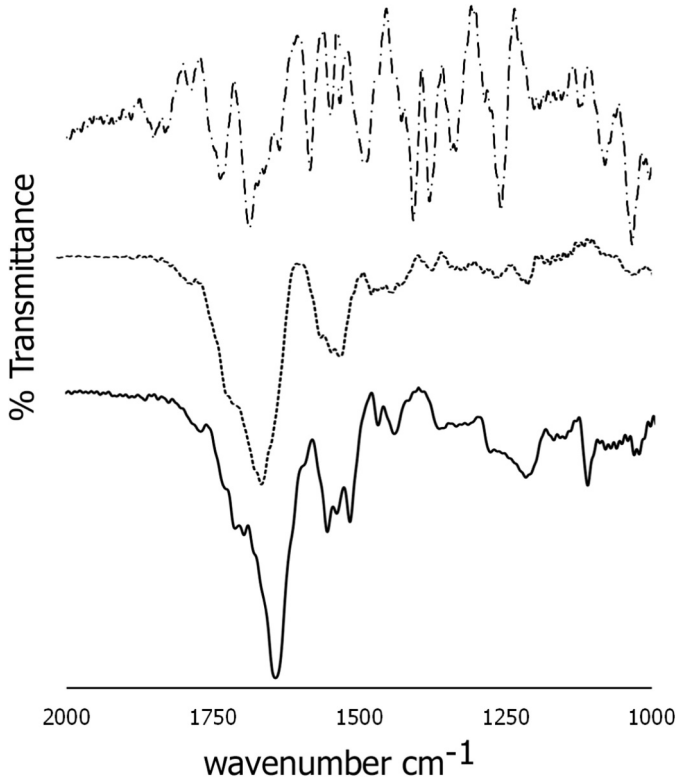

Figure 6. Comparison of FTIR spectra of W-C4-W assemblies (top); W-C4-W assemblies bound to collagen (middle); W-C4-W assemblies bound to collagen and tenascin (bottom).

171.9°C) due to thermal melting and decomposition, however, were observed. These results further confirm the formation of the composite scaffolds.

Rheological Properties of Scaffold

Rheological properties of the scaffold can provide critical information about the viscoelastic behavior and the impact of collagen and tenascin-X on the scaffold. Frequency sweep tests provide valuable information about the mechanical strength of the scaffold due to interactions between the components of the scaffold and degree of dispersion. We examined the storage and loss modulus as well as the complex viscosity (Fig. 8) at varying strain percentages. The complex viscosity of the scaffold with tenascin and collagen-bound assemblies decreases with frequency (Fig. 8a). Moreover, higher complex viscosity values are observed at lower frequencies and at lower strain %. These results indicate that at higher frequencies, there is a reduction in hydrogen-bonding interactions, leading to a disentanglement of chains within the scaffold and possible loosening of the network at higher frequencies. Additionally, this effect is higher when the strain is increased, which is expected. Similar behavior has been seen in the case of gelatin-based hydrogels.[78] Fig. 8(b) shows the storage modulus (G') and loss modulus (G") of the scaffold at 1%, and 5% strain. As can be seen, the storage modulus of the scaffold increased as the frequency increased and then stabilized after 2 rads/s, additionally, the storage modulus was higher at each of the strain values applied compared to the loss modulus indicating the elasticity of the scaffold. Furthermore, as expected, higher storage and loss modulus values were seen at lower % strain. This behavior of the storage modulus is due to a higher resistance to deformation as the frequency is increased as the scaffold components have lesser time to relax between cycles. We then compared the mechanical properties of the scaffold without tenascin-X. As seen in Fig. 8(c), the complex viscosity showed a similar trend as that seen for the composite with tenascin-X in that the complex viscosity decreased at higher frequencies, however, the values were lower compared to the composite scaffold with tenascin-X. The corresponding results for storage and loss modulus (Fig. 8d) show that at 1% strain, the storage modulus and loss modulus showed an initial increase after which the values leveled off at higher frequencies. However, at 5% strain, the values continued to increase at higher frequencies. The loss modulus was once again lower than the storage modulus indicating that the scaffolds formed without tenascin also displayed elastic properties. Furthermore, the storage and loss modulus values were higher at lower strain percentages as expected. Overall, the storage modulus values were higher after

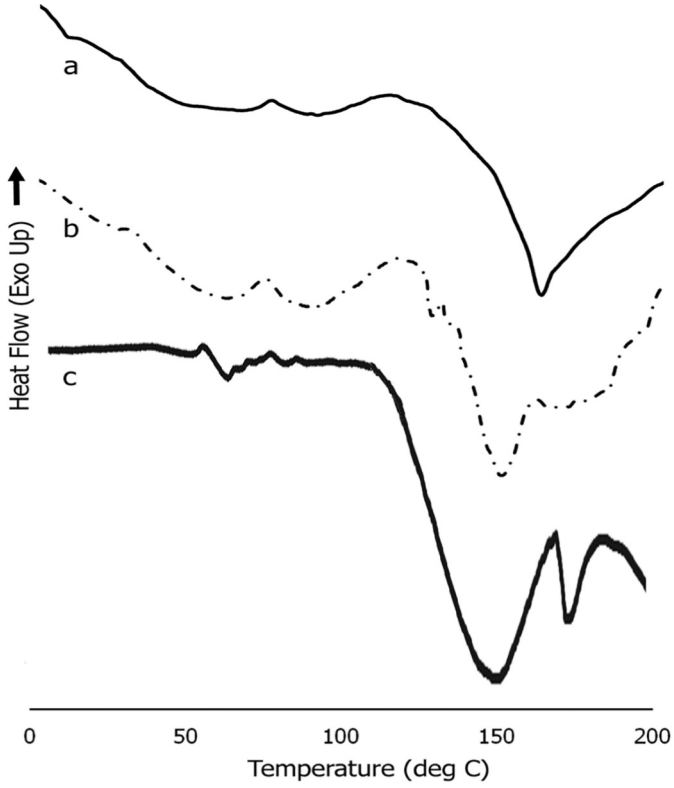

Figure 7. DSC analysis (a) W-C4-W assemblies; (b) W-C4-W assemblies bound to collagen; (c) W-C4-W assemblies bound to collagen and tenascin.

incorporation of tenascin-x, which is attributed to higher cross-linking under those conditions.

Biodegradability Studies

The biodegradability of a scaffold is known to play an important role to allow for the gradual replacement of the ECM over time and thus is critical for proper growth of tissue.[79] We examined the biodegradability of the scaffold over a period of 2 weeks (Fig. 9). As can be seen the scaffold showed biodegradability over time, and after a period of 2 weeks, the percent weight loss was found to be 41.5%, thus confirming the biodegradability of the scaffold.

Antioxidant Activity

In general, it is well known that physiologically tissues are exposed to extrinsic and intrinsic oxidative stress as a result of free-radical damage.[80] Scaffolds with antioxidant activities may aid in reducing oxidative stress that may lead to diseases. We thus examined if the formed scaffold displayed antioxidant activity by conducting DPPH radical scavenging assay. Our results (Fig. 10) indicate that the biocomposite scaffold displayed a concentration dependent antioxidant activity. This may be attributed to the fact that peptide-based scaffold contains components that display radical scavenging activity.

Cell Studies

To examine cellular viability in the presence of the scaffold, we conducted MTT assays in the presence of keratinocytes (Fig. 11). As can be seen, in Figure 11a, at low concentrations, no cytotoxicity was observed, while at higher concentrations, in general over 81% of the cells were found to be viable. These results demonstrated overall low cytotoxicity of the scaffold even at relatively higher concentrations. In previous work, it was shown that scaffolds demonstrating a viability of >80% are considered to be relatively non-cytotoxic.[81] We also carried out optical microscopy of the cells in the presence of the scaffold (Fig. 11b). As can be seen, the cells were found to adhere to the scaffolds and overall increased cell spreading and formation of cell-scaffold matrices was observed further confirming that the cells continued to thrive in the presence of the scaffold.

Cell Proliferation and Growth within Bioprinted Scaffolds

After confirmation of cytocompatibility of the cells in the presence of the 2D scaffolds, in order to create three-dimensional scaffolds, the biocomposites were bioprinted

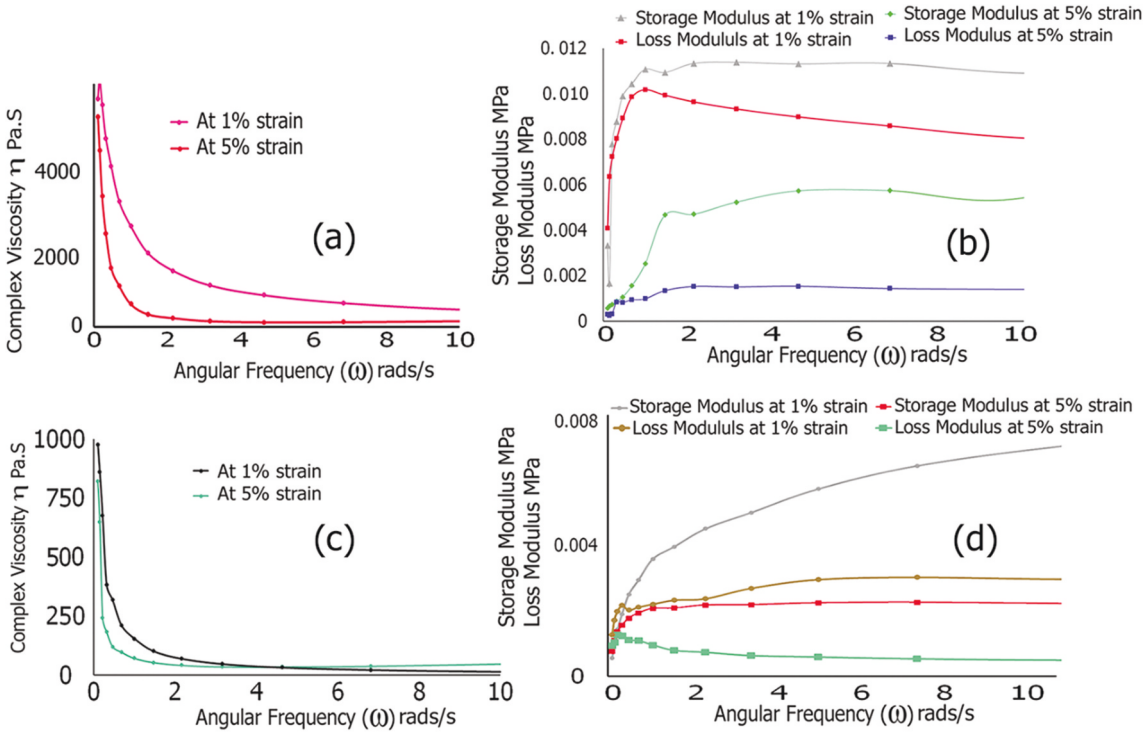

Figure 8. Frequency sweep analysis of scaffolds before and after incorporation of tenascin X at 5% and 1% strain. (a) Complex viscosity analyses of W-C4-W assemblies with collagen and tenascin-x; (b) storage and loss modulus analysis of W-C4-W assemblies with collagen and tenascin-x; (c) (a) complex viscosity analyses of W-C4-W assemblies with collagen; (d) storage and loss modulus analysis of W-C4-W assemblies with collagen.

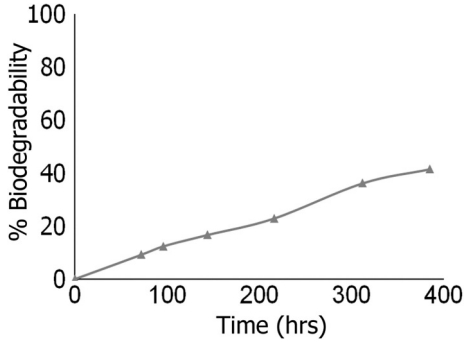

Figure 9. Percent biodegradability of the scaffold W-C4-W assemblies bound to collagen and tenascin-X.

using droplet bioprinting in the presence of co-cultures of human dermal fibroblasts and keratinocytes. Given the antioxidant activity of the scaffolds, those cell lines were selected given their importance in order to potentially create 3D scaffolds that may be applicable in skin tissue regeneration.[82] The optical microscopy images of the bioprinted scaffolds obtained through droplet bioprinting are shown in Figure 12. As can be seen, over time, the cells were found to proliferate and grow not only within the bioprinted scaffold but also continued to form hierarchical cell-to-cell networks around the scaffold. These results further confirm that the bioprinted scaffold not only promotes cell adhesion but also is conducive cell – cell interactions that are essential for tissue-engineered scaffolds.

Cytoskeletal Studies

To further investigate the impact of the bioprinted scaffold, on the actin cytoskeleton of the cells, we conducted FITC labeled phalloidin assays which allowed for staining of F-actin filaments of the cells within the bioprinted scaffolds.[83] As seen in Fig. 13, cells were found to spread within the scaffold and appeared elongated with extended actin filaments. Well-defined elongated focal adhesions were observed. Previously, it has been reported that a spatial relationship between actin cytoskeletal morphology and focal contacts in fibroblasts have been observed depending upon cell-to-substrate contacts and cytoskeletal organization which not only dictates cell adhesion but also motility.[84] Furthermore, cell motility and spreading are key processes that are governed by the dynamics of the cytoskeletal protein actin. After 3 days, cell membrane ruffling is observed with lamellopidia protrusions at the leading edge of the cells which are crucial for cell migration. After 6 days, long extended filopodia are also seen, further confirming that the cells were found to maintain their migratory capability and spread within the bioprinted scaffold. Thus, our results suggest that the bioprinted scaffolds

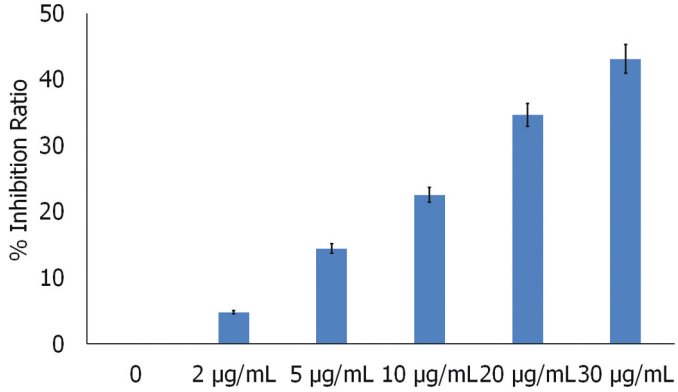

Figure 10. Comparison of DPPH inhibition ratio at varying concentrations of the W-C4-W-collagen-tenascin-X scaffold.

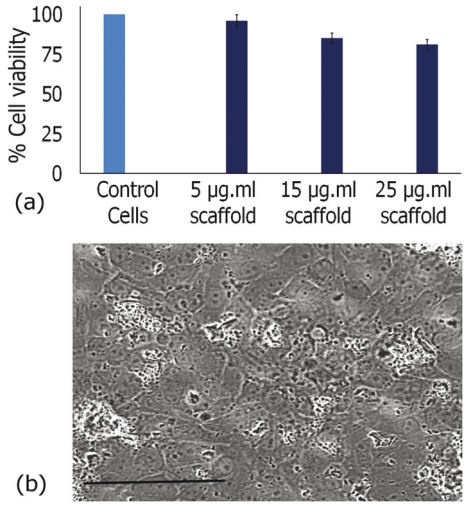

Figure 11. (a) Percent cell viability of keratinocytes at varying concentrations of scaffold consisting of W-C4-W-assemblies bound to collagen and tenascin-X. ($n = 3$, $p < .05$) (b) optical microscopy image of proliferating cells over a period of 48 hours forming cell-scaffold matrices. Scale bar = 25 µm.

not only allowed for efficient cell – scaffold interactions and therefore may have enhanced functionality in tissue engineering and potential regenerative medicine applications.

Conclusions

In this work, we have designed new peptide sequences and peptide bolaamphiphiles which were predicted to have antioxidant properties computationally. Two of those peptides were further utilized to create new peptide bolaamphiphiles. The ability of the peptides and the bolaamphiphiles to form supramolecular assemblies was then investigated using replica modeling molecular dynamics. Results indicated structural changes during association or dissociation of the assemblies, over the simulation period. In general, uniform clusters were seen at the end of the simulation in all cases except the GADIVA peptide. Overall, π-π stacking interactions and hydrogen bonds played a key role in the formation of most assemblies that formed fibrous or spherical clusters. As a proof of concept, we synthesized the bolaamphiphile W-C4-W and investigated its self-assembly process, which showed the formation of fibrous nanoassemblies. The nanoassemblies were then further conjugated with collagen and tenascin-X that resulted in a gelatinous crosslinked fibrous mesh. The antioxidant properties of the scaffold was studied using DPPH assay, which revealed that

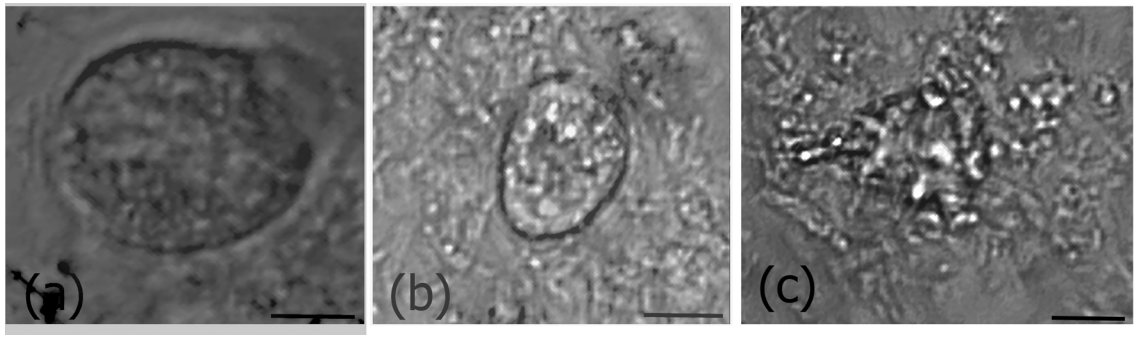

Figure 12. Bioprinted scaffold with co-cultured cells of fibroblasts and keratinocytes. (a) after 24 hours; (b) after 48 hours; (c) after six days. Scale bar = 25 µm.

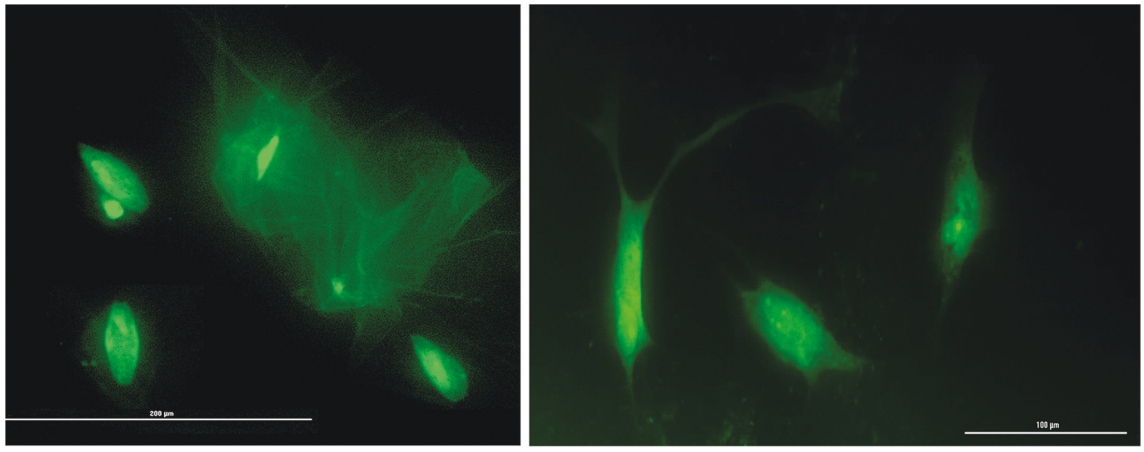

Figure 13. Confocal images of co-cultured fibroblasts and keratinocytes grown within the bioprinted scaffold. After three days of growth (Left); after six days (Right).

the scaffold demonstrated concentration dependent antioxidant activity. The scaffold was then utilized along with co-cultures of human dermal fibroblasts and keratinocytes for bioprinting. The formed 3D scaffolds were found to be biocompatible, and actin cytoskeletal studies revealed the formation of lamellopodia and elongated filopodia within the bioprinted matrix, thus affirming the migratory ability of the cells. Overall, these studies reveal that the supramolecular assemblies formed using the bolaamphiphile may have potential applications in tissue engineering applications and may also be potentially utilized for cell encapsulation and other therapeutic applications.

Acknowledgments

The authors thank Upendar Thaduri and Andrew Angelopoulos from the Advanced Research Computing, Education Technologies and Research Computing Department at Fordham University, a division of the Office of Information Technology for providing their assistance and access to research computing resources that have contributed to the computational results reported here.

Disclosure Statement

No potential conflict of interest was reported by the author(s).

Funding

IB thanks NSF-MRI grants 1626378 and 2117625 as well as Fordham University research grants for financial support. MB and HH thank the Henry Luce Foundation for Clare Boothe Luce Scholarships that helped fund this work. MB also thanks the Blavatnik Foundation and the Barry Goldwater Scholarship for financial support.

Data Availability Statement

The authors declare that the supporting data and the findings of this study are available within the article and its Supplementary Information.

References

[1] Stupp, S. I.; Zha, R. H.; Palmer, L. C.; Cui, H.; Bitton, R. Self-Assembly of Biomolecular Soft Matter. *Faraday Discuss.* 2013, *166*, 9–30. DOI: 10.1039/c3fd00120b.

[2] Belluati, A.; Sètuhn, J.; Chadwick, R.; Glynn, C.; Chami, M.; Happel, D.; Guo, C.; Kolmar, H.; Bruns, N. Artificial Cell Synthesis Using Biocatalytic Polymerization-Induced Self-Assembly. *Nat. Chem.* 2024, *16*(4), 564–574. DOI: 10.1038/s41557-023-01391-y.

[3] Yadav, S.; Sharma, A. K.; Kumar, P. Nanoscale Self-Assembly for Therapeutic Drug Delivery. *Front. Bioeng. Biotechnol.* 2020, *8*. DOI: 10.3389/fbioe.2020.00127.

[4] Wang, Z. L.; Song, J. Piezoelectric Nanogenerators Based on Zinc Oxide Nanowire Arrays. *Science* 2006, *312*(5771), 242–246. DOI: 10.1126/science.1124005.

[5] Roy, A.; Shrivastava, S.; Mandal, S. Self-Assembled Carbohydrate Nanostructures: Synthesis Strategies to Functional Application in Food. Chp. 5. In Nanotechnology in the Agri-Food Industry, Novel Approaches of Nanotechnology in Food, Grumezescu, A. M., Ed.; Academic Press: London, UK, 2016; Vol. 1, pp. 133–164.

[6] Astanina, K.; Koch, M.; Jüngst, C.; Zumbusch, A.; Kiemer, A. K. Lipid Droplets as a Novel Cargo of Tunnelling Nanotubes in Endothelial Cells. *Sci. Rep.* 2015, *5*(1), 11453. DOI: 10.1038/srep11453.

[7] Kamada, A.; Rodriguez-Garcia, M.; Ruggeri, F. S.; Shen, Y.; Levin, A.; Knowles, T. Controlled Self-Assembly of Plant Proteins into

High-Performance Multifunctional Nanostructured Films. *Nat. Commun.* 2021, *12*(1), 3529. DOI: 10.1038/s41467-021-23813-6.

[8] Ghosh, M.; Halperin-Sternfel, M.; Grigoiants, I.; Lee, J.; Nam, K.; Alder-Abramovich, L. Arginine-Presenting Peptide Hydrogels Decorated with Hydroxyapatite as Biomimetic Scaffolds for Bone Regeneration. *Biomacromolecules* 2017, *18*(11), 3541–3550. DOI: 10.1021/acs.biomac.7b00876.

[9] Brito, A.; Kassem, S.; Reis, R.; Uljin, R.; Pires, R.; Pashkuleva, I. Carbohydrate Amphiphiles for Supramolecular Biomaterials: Design, Assembly and Applications. *Chem.* 2021, *7*(11), 2943–2964. DOI: 10.1016/j.chempr.2021.04.011.

[10] Fu, I.; Markegrad, C.; Chu, B.; Nguyen, H. D. Role of Hydrophobicity on Self-Assembly by Peptide Amphiphiles via Molecular Dynamics Simulations. *Langmuir* 2014, *30*(26), 7745–7754. DOI: 10.1021/la5012988.

[11] Willams-Noonan, B.; Kamboukos, A.; Todorva, N.; Yarovksy, I. Self-Assembling Peptide Biomaterials: Insights from Spontaneous and Enhanced Sampling Molecular Dynamics Simulation. *Chem. Phys. Rev.* 2023, *4*(2), 021304. DOI: 10.1063/5.0142302.

[12] Lee, O.-S.; Stupp, S. I.; Schatz, G. C. Atomistic Molecular Dynamics Simulations of Peptide Amphiphile Self-Assembly into Cylindrical Nanofibers. *J. Am. Chem. Soc.* 2011, *133*(10), 3677–3683. DOI: 10.1021/ja110966y.

[13] Xiong, Q.; Stupp, S. I.; Schatz, G. C. Molecular Insight into the β-Sheet Twist and Related Morphology of Self-Assembled Peptide Amphiphile Ribbons. *J. Phys. Chem. Lett.* 2021, *12*(46), 11238–11244. DOI: 10.1021/acs.jpclett.1c03243.

[14] Xiong, Q.; Jiang, Y.; Cai, X.; Yang, F.; Li, Z.; Han, W. Conformation Dependence of Diphenylalanine Self-Assembly Structures and Dynamics: Insights from Hybrid-Resolution Simulations. *ACS Nano*. 2019, *13*(4), 4455–4468. DOI: 10.1021/acsnano.8b09741.

[15] Esteben-Martin, S.; Salgado, J. Self-Assembling of Peptide-Membrane Complexes by Atomistic Molecular Dynamics Simulations. *Biophys. J.* 2007, *92*(3), 903–912. DOI: 10.1529/biophysj.106.093013.

[16] Chen, S.; Lin, T.; Basu, R.; Ritchey, J.; Wang, S.; Luo, Y.; Li, X.; Pei, D.; Kara, L.; Cheng, X. Design of Target Specific Peptide Inhibitors Using Generative Deep Learning and Molecular Dynamics Simulations. *Nat. Commun.* 2024, *15*(1), 1611. DOI: 10.1038/s41467-024-45766-2.

[17] Knapp, B.; Demharter, S.; Esmaielbeiki, R.; Deane, C. M. Current Status and Future Challenges in T-Cell Receptor/Peptide/MHC Molecular Dynamics Simulations. *Brief Bioinform* 2015, *16*(6), 1035–1044. DOI: 10.1093/bib/bbv005.

[18] Kahler, U.; Fuchs, J. E.; Goettig, P.; Liedl, K. R. An Unexpected Switch in Peptide Binding Mode: From Simulation to Substrate Specificity. *J. Biomol. Struct. Dyn.* 2018, *36*(15), 4072–4084. DOI: 10.1080/07391102.2017.1407674.

[19] Lee, H.; Heo, L.; Lee, M. S.; Seok, C. GalaxyPepdock: A Protein–Peptide Docking Tool Based on Interaction Similarity and Energy Optimization. *Nucleic Acids Res.* 2015, *43*(W1), W431–W435. DOI: 10.1093/nar/gkv495.

[20] Sugita, Y.; Okamoto, Y. Replica-Exchange Molecular Dynamics Method for Protein Folding. *Chem. Phys. Lett.* 1999, *314*(1–2), 141–151. DOI: 10.1016/S0009-2614(99)01123-9.

[21] Xi, R.; Wei, G.; Ma, B.; Nussinov, R. Replica Exchange Molecular Dynamics: A Practical Application Protocol with Solutions to Common Problems and a Peptide Aggregation and Self-Assembly Example. *Methods Mol. Biol.* 2018, *1777*, 101–119.

[22] Cao, Z.; Liu, L.; Wu, P.; Wang, J. Structural and Thermodynamics Characters of Isolated α-syn12 Peptide: Long-Time Temperature Replica-Exchange Molecular Dynamics in Aqueous Solution. *Acta Biochim. Biophys. Sin.* 2011, *43*(3), 172–180. DOI: 10.1093/abbs/gmr002.

[23] Patel, S.; Hosur, R. Replica Exchange Molecular Dynamics Simulations Reveal Self-Association Sites in M-Crystallin Caused by Mutations Provide Insights of Cataract. *Sci. Rep.* 2021, *11*(1), 23270. DOI: 10.1038/s41598-021-02728-8.

[24] Yang, X.-R.; Zhao, Y.-Q.; Qiu, Y.-T.; Chu, C.-F.; Wang, B. Preparation and Characterization of Gelatin and Antioxidant Peptides from Gelatin Hydrolysate of Skipjack Tuna (Katsuwonus Pelamis) Bone Stimulated by in vitro Gastrointestinal Digestion. *Mar. Drugs* 2019, *17*(2), 78. DOI: 10.3390/md17020078.

[25] Zhang, J. B.; Wang, Y. M.; Chi, C. F.; Sun, K. L.; Wang, B. Eight Peptides from Collagen Hydrolysate Fraction of Spanish Mackerel (*Scomberomorous niphonius*) Skin: Isolation, Identification, and Antioxidant Activity in vitro. *Mar. Drugs* 2019, *17*(4), 224. DOI: 10.3390/md17040224.

[26] Wu, R.; Wu, C.; Liu, D.; Yang, X.; Huang, J.; Zhang, J.; Liao, B.; He, H. Antioxidant and Antifreezing Peptides from Salmon Collagen Hydrolysate Prepared by Bacterial Extracellular Protease. *Food Chem.* 2018, *248*, 346–352. DOI: 10.1016/j.foodchem.2017.12.035.

[27] Xu, N.; Chen, G.; Liu, H. Antioxidative Categorization of Twenty Amino Acids Based on Experimental Evaluation. *Molecules* 2017, *22*(12), 2066. DOI: 10.3390/molecules22122066.

[28] Aguilar-Toala, J.; Liceaga, A. Cellular Antioxidant Effect of Bioactive Peptides and Molecular Mechanisms Underlying: Beyond Chemical Properties. *Int. J. Food Sci. Technol.* 2021, *56*(5), 2193–2204. DOI: 10.1111/ijfs.14855.

[29] Olsen, T. H.; Yesiltas, B.; Isa Marin, F.; Perseva, M.; Garica-Moreno, P.; Gregersen, S.; Overgaard, M. T.; Jacobsen, C.; Lund, O.; Hansen, E. B., et al. AnOxpepred: Using Deep Learning for the Prediction of Antioxidative Properties of Peptides. *Sci. Rep.* 2020, *10*(1), 21471. DOI: 10.1038/s41598-020-78319-w.

[30] Balasubramanian, P.; Prabhakaran, M. P.; Sireesha, M.; Ramakrisha, S. C. Collagen in Human Tissues: Structure, Function and Biomedical Applications from a Tissue Engineering Perspective. In *Polymer Composites—Polyolefin-fractionation-polymeric Peptidomimetics — Collagens*, Abe, A., Kausch, H. H., Moller, M. Paschi, H., Eds.; Springer: Berlin/Heidelberg, Germany, 2013; Vol. 251, pp. 173–206. Advances in Polymer Science.

[31] Dong, C.; Lv, Y. Application of Collagen Scaffold in Tissue Engineering: Recent Advances and New Perspectives. *Polymers* 2016, *8*(2), 42. DOI: 10.3390/polym8020042.
[32] Sundar, G.; Joseph, J. C. P.; John, A. Natural Collagen Bioscaffolds for Skin Tissue Engineering Strategies in Burns: A Critical Review. *Int. J. Polym. Mater. Polym. Biomater.* 2020, *70*(9), 593–604. DOI: 10.1080/00914037.2020.1740991.
[33] Shoulders, M. D.; Raines, R. T. Collagen Structure and Stability. *Annu. Rev. Biochem.* 2009, *78*(1), 929–958. DOI: 10.1146/annurev.biochem.77.032207.120833.
[34] Valcourt, U.; Alcaraz, L. B.; Exposito, J. Y.; Lethias, C.; Bartholin, L. Tenascin-X: Beyond the Architectural Function. *Cell. Adh. Migr.* 2015, *9*(1–2), 154–165. DOI: 10.4161/19336918.2014.994893.
[35] Okuda-Ashitaka, E.; Matsumoto, K. I. Tenascin-X as a Causal Gene for Classical-Like Ehlers-Danlos Syndrome. *Front Genet.* 2023, *14*, 1107787. DOI: 10.3389/fgene.2023.1107787.
[36] Mao, J. R.; Taylor, G.; Dean, W. B.; Wagner, D. R.; Afzal, V.; Lotz, J. C.; Rubin, E. M.; Bristow, J. Tenascin-X Deficiency Mimics Ehlers-Danlos Syndrome in Mice Through Alteration of Collagen Deposition. *Nat. Genet.* 2002, *30*(4), 421–425. DOI: 10.1038/ng850.
[37] Schrödinger, L.; DeLano, W. *PyMOL*. 2020. http://www.pymol.org/pymol.
[38] Yan, R.; Xu, D.; Yang, J.; Walker, S.; Zhang, Y. A Comparative Assessment and Analysis of 20 Representative Sequence Alignment Methods for Protein Structure Prediction. *Sci. Rep.* 2013, *3*(1), 2619. DOI: 10.1038/srep02619.
[39] Jumper, J.; Evans, R.; Pritzel, A.; Green, T.; Figurnov, M.; Ronneberger, O.; Tunyasuvunakool, K.; Bates, R.; Zidek, A.; Potapenko, A., et al. Highly Accurate Protein Structure Prediction with AlphaFold. *Nature* 2021, *596*(7873), 583–589. DOI: 10.1038/s41586-021-03819-2.
[40] Abramson, J.; Adler, J.; Dunger, J.; Evans, R.; Green, T.; Pritzel, A.; Ronneberger, O.; Willmore, L.; Ballard, A.; Bambrick, J., et al. Accurate Structure Prediction of Biomolecular Interactions with AlphaFold 3. *Nature* 2024, *630*(8016), 493–500. DOI: 10.1038/s41586-024-07487-w.
[41] Xu, J.; Zhang, Y. How Significant is a Protein Structure Similarity with TM-Score = 0.5? *Bioinformatics*. 2010, *26*(7), 889–895. DOI: 10.1093/bioinformatics/btq066.
[42] Bowers, K. J.; Chow, E.; Xu, H.; Dror, R. O.; Eastwood, M. P.; Gregersen, B. A.; Klepeis, J. L.; Kolossvary, I.; Moraes, M. A.; Sacerdoti, F. D., et al. Scalable Algorithms for Molecular Dynamics Simulations on Commodity Clusters. *Proc. ACM/IEEE Conference on Supercomputing (SC06)*, Tampa, Florida, Nov 11–17, 2006.
[43] Yang, X.; Zhu, Y.; Ye, S.; Zhang, R.; Lu, L. Structure of a Triple-Helix Region of Human Collagen Type II. To be published. https://www.rcsb.org/structure/6jec .
[44] Ohnishi, S.; Kigawa, T.; Tochion, N.; Koshiba, S.; Inoue, M.; Yokoyama, S. Solution Structure of the 31st Fibronectin Type III Domain of the Human Tenascin X. To be published. https://www.rcsb.org/structure/2CUI.
[45] Eberhardt, J.; Santos-Martins, D.; Tillack, A. F.; Forli, S. AutoDock Vina 1.2.0: New Docking Methods, Expanded Force Field, and Python Bindings. *J. Chem. Inf. Modeling* 2021, *61*(8), 3891–3898. DOI: 10.1021/acs.jcim.1c00203.
[46] Trott, O.; Olson, A. J. AutoDock Vina: Improving the Speed and Accuracy of Docking with a New Scoring Function, Efficient Optimization, and Multithreading. *J. Comput. Chem.* 2010, *31*(2), 455–461. DOI: 10.1002/jcc.21334.
[47] Salentin, S.; Schreiber, S.; Haupt, V.; Adasme, M.; Schroeder, M. PLIP: Fully Automated Protein–Ligand Interaction Profiler. *Nucleic Acids Res.* 2015, *43*(W1), W443–W447. DOI: 10.1093/nar/gkv315.
[48] Fischer, M. J. E. Amine Coupling Through EDC/NHS: A Practical Approach. In Surface Plasmon Resonance. *Methods in Molecular Biology*, Mol, N., and Fischer, M., Eds.; Humana Press: Totowa, NJ, 2010; Vol. 627, pp. 55–73.
[49] Gulcin, İ.; Alwasel, S. DPPH Radical Scavenging Assay. *Processes*. 2023, *11*(8), 11, 2248. DOI: 10.3390/pr11082248.
[50] Kokubo, T.; Kushitani, H.; Sakka, S.; Kitsugi, T.; Yamamuro, T. Solutions Able to Reproduce in vivo Surface-Structure Changes in Bioactive Glass-Ceramic A-W 3. *J. Biomed. Mater. Res.* 1990, *24*(6), 721–734. DOI: 10.1002/jbm.820240607.
[51] van Meerloo, J.; Kaspers, G.; Cloos, J. Cell Sensitivity Assays: The MTT Assay. *Methods Mol. Biol.* 2011, *731*, 237–245.
[52] Gudapati, H.; Dey, M.; Ozbolat, I. A Comprehensive Review on Droplet-Based Bioprinting: Past, Present and Future. *Biomaterials*. 2016, *102*, 20–42. DOI: 10.1016/j.biomaterials.2016.06.012.
[53] Huo, X.; Xu, X.-J.; Chen, Y.-W.; Yang, H.-W.; Piao, Z.-X. Filamentous-Actins in Human Hepatocarcinoma Cells with CLSM. *World J. Gastroenterol.* 2004, *10*(11), 1666–1668. DOI: 10.3748/wjg.v10.i11.1666.
[54] Zheng, L.; Zhao, Y.; Dong, H.; Su, G.; Zhao, M. Structure–Activity Relationship of Antioxidant Dipeptides: Dominant Role of Tyr, Trp, Cys and Met Residues. *J. Funct. Foods* 2016, *21*, 485–496. DOI: 10.1016/j.jff.2015.12.003.
[55] Smoak, E.; Carlo, A.; Fowles, C.; Banerjee, I. A. Self-Assembly of Gibberellic Amide Assemblies and Their Applications in the Growth and Fabrication of Ordered Gold Nanoparticles. *Nanotechnol.* 2010, *21*(2), 025603. DOI: 10.1088/0957-4484/21/2/025603.
[56] Bhattacharjee, N.; Biswas, P. Position-Specific Propensities of Amino Acids in the β-Strand. *BMC Struc. Biol.* 2010, *10*(1), 29. DOI: 10.1186/1472-6807-10-29.
[57] Ruff, K. M.; Pappu, R. V. AlphaFold and Implications for Intrinsically Disordered Proteins. *J. Mol. Biol.* 2021, *433*(20), 167208. DOI: 10.1016/j.jmb.2021.167208.
[58] Ramachandran, S.; Kota, P.; Ding, F.; Dokholyan, N. Automated Minimization of Steric Clashes in Protein Structures. *Proteins*. 2011, *79*(1), 261–270. DOI: 10.1002/prot.22879.
[59] Richmond, T. Solvent Accessible Surface Area and Excluded Volume in Proteins. Analytical Equations for Overlapping Spheres and Implications for the Hydrophobic Effect. *J. Mol. Biol.* 1984, *178*(1), 63–89. DOI: 10.1016/0022-2836(84)90231-6.

[60] Rashid, H.; Ahmad, N.; Abdalla, M.; Khan, K.; Martines, M. A.; Shabana, S. Molecular Docking and Dynamic Simulations of Cefixime, Etopside and Nebrodenside a Against the Pathogenic Proteins of SARS-COV-2. *J. Mol. Struct.* 2022, *1247*, 131296. DOI: 10.1016/j.molstruc.2021.131296.

[61] Ferdausi, N.; Islam, S.; Rimti, F.; Quayum, S.; Arshad, E.; Ibnat, A.; Islam, T.; Arefin, A.; Ema, T.; Biswas, P., et al. Point-Specific Interactions of Isovitexin with the Neighboring Amino Acid Residues of the hAce2 Receptor as a Targeted Therapeutic Agent in Suppressing the SARS-CoV-2 Influx Mechanism. *J. Adv. Vet. Anim. Res.* 2022, *9*(2), 230–240. DOI: 10.5455/javar.2022.i588.

[62] Mazola, Y.; Guirola, O.; Palomares, S.; Chinea, G.; Menéndez, C.; Hernández, L.; Musacchio, A. A Comparative Molecular Dynamics Study of Thermophilic and Mesophilic β-Fructosidase Enzymes. *J. Mol. Model.* 2015, *21*(9), 1–11. DOI: 10.1007/s00894-015-2772-4.

[63] Bhattacharya, R.; Saha, R.; Samanta, U.; Chakrabarti, P. Geometry of Interaction of the Histidine Ring with Other Planar Basic Residues. *J. Proteome. Res.* 2003, *2* (3), 255–263. DOI: 10.1021/pr025584d.

[64] Ermilova, I.; Lyubartsev, A. P. Modelling of Interactions Between Aβ(25–35) Peptide and Phospholipid Bilayers: Effects of Cholesterol and Lipid Saturation. *RSC Adv.* 2020, *10*(7), 3902–3915. DOI: 10.1039/C9RA06424A.

[65] Heise, R. M.; Banerjee, I. A. Design of Short Peptide and Peptide Amphiphiles as Collagen Mimics and an Investigation of Their Interactions with Collagen Using Molecular Dynamics Simulations and Docking Studies. *J. Mol. Model* 2023, *29*(1), 19. DOI: 10.1007/s00894-022-05419-x.

[66] Kumar, P.; Satyam, A.; Fan, X.; Collin, E.; Rochev, Y.; Rodriguez, R.; Gorelov, A.; Dillon, S.; Joshi, L.; Raghunath, M., et al. Macromolecularly Crowded in vitro Microenvironments Accelerate the Production of Extracellular Matrix-Rich Supramolecular Assemblies. *Sci. Rep.* 2015, *5*(1), 8729. DOI: 10.1038/srep08729.

[67] Elefteriou, F.; Exposito, J.-Y.; Garrone, R.; Lethias, C. Characterization of the Bovine-Tenascin-X. *J. Biol. Chem.* 1997, *272*(36), 22866–22874. DOI: 10.1074/jbc.272.36.22866.

[68] Przybyłek, M.; Bełdowski, P.; Wieland, F.; Cysewski, P.; Sionlowska, A. Collagen Type II—Chitosan Interactions as Dependent on Hydroxylation and Acetylation Inferred from Molecular Dynamics Simulations. *Molecules* 2023, *28*(1), 154. DOI: 10.3390/molecules28010154 .

[69] Mosseri, A.; Sancho-Albero, M.; Mercurio, F.; Leone, M.; DeCola, L.; Romanelli, A. Tryptophan-PNA Gc Conjugates Self-Assemble to Form Fibers. *Bioconj. Chem.* 2023, *34*(8), 1429–1438. DOI: 10.1021/acs.bioconjchem.3c00200.

[70] Khemaissa, S.; Sagan, S.; Walrant, A. Tryptophan, an Amino-Acid Endowed with Unique Properties and Its Many Roles in Membrane Proteins. *Crystals* 2021, *11* (9), 1032. DOI: 10.3390/cryst11091032.

[71] Przybyla, D. E.; Chmielewski, J. Higher-Order Assembly of Collagen Peptides into Nano- and Microscale Materials. *Biochemistry*. 2010, *49*(21), 4411–4419. DOI: 10.1021/bi902129p.

[72] Miller, J. L. Tenascin-X Discovery and Early Research. *Front. Immunol.* 2020, *11*, 612497. DOI: 10.3389/fimmu.2020.612497.

[73] Ramamurthy, N.; Kannan, S. Fourier Transform Infrared Spectroscopic Analysis of a Plant (Calotropis Gigantea Linn) from an Industrial Village, Cuddalore Dt. Tamil Nadu, India. *Rom. J. Biophys.* 2007, *17*, 269–276.

[74] Belbachir, K.; Noreen, R.; Gouspillou, G.; Petibois, C. Collagen Types Analysis and Differentiation by FTIR Spectroscopy. *Anal. Bioanal. Chem.* 2009, *395*(3), 829–837. DOI: 10.1007/s00216-009-3019-y.

[75] Derenne, A.; Derfoufi, K.-M.; Cowper, B.; Delporte, C.; Butre, C.; Goormaghtigh, E. Analysis of Glycoproteins by ATR-FTIR Spectroscopy: Comparative Assessment. *Methods Mol. Biol.* 2021, *2271*, 361–374.

[76] Arakawa, K.; Numata, K. Reconsidering the "Glass Transition" Hypothesis of Intrinsically Unstructured CAHS Proteins in Desiccation Tolerance of Tardigrades. *Molecular Cell* 2020, *81*(3), 409–410. DOI: 10.1016/j.molcel.2020.12.007.

[77] Bozec, L.; Odlyha, M. Thermal Denaturation Studies of Collagen by Microthermal Analysis and Atomic Force Micrsocopy. *Biophys. J.* 2011, *101*(1), 228–236. DOI: 10.1016/j.bpj.2011.04.033.

[78] Kokol, V.; Pottathara, Y. B.; Mihelcic, M.; Perse, L. S. Rheological Properties of Gelatine Hydrogels Affected by Flow- and Horizontally-Induced Cooling Rates During 3D Cryo-Printing. *Coll. Surfaces. A* 2021, *616*, 126356. DOI: 10.1016/j.colsurfa.2021.126356.

[79] Bitar, K.; Zakhem, E. Design Strategies of Biodegradable Scaffolds for Tissue Regeneration. *Biomed. Eng. Comput. Biol.* 2014, *6*, 13–20. DOI: 10.4137/BECB.S10961.

[80] Chaudhary, P.; Janmeda, P.; Docea, A.; Yeskaliyeva, B.; Razis, A.; Modu, B.; Calina, D.; Sharifi-Rad, J. Oxidative Stress, Free Radicals and Antioxidants: Potential Crosstalk in the Pathophysiology of Human Diseases. *Front. Chem.* 2023, *11*, 1158198. DOI: 10.3389/fchem.2023.1158198.

[81] Gogele, C.; Wiltzsch, S.; Lenhart, A.; Civilleri, A.; Weiger, T.; Schafer-Eckart, K.; Minnich, B.; Forchheimer, L.; Hornfeck, M.; Schulze-Tanzil, G. Highly Porous Novel Chondro-Instructive Bioactive Glass Scaffolds Tailored for Cartilage Tissue Engineering. *Mater. Sci. Eng. C* 2021, *130*, 112421. DOI: 10.1016/j.msec.2021.112421.

[82] Russo, B.; Brembilla, N.; Chizzolini, C. Interplay Between Keratinocytes and Fibroblasts: A Systematic Review Providing a New Angle for Understanding Skin Fibrotic Disorders. *Front. Immunol.* 2020, *11*, 648. DOI: 10.3389/fimmu.2020.00648.

[83] Romani, M.; Auwerx, J. Phalloidin Staining of Actin Filaments for Visualization of Muscle Fibers in Caenorhabditis Elegans. *Bio. Protoc.* 2021, *11*(19), e4183. DOI: 10.21769/BioProtoc.4183.

[84] Thoumine, O.; Ott, A. Influence of Adhesion and Cytoskeletal Integrity on Fibroblast Traction. *Cell. Mot. Cytoskeleton* 1996, *35*(3), 269–280. DOI: 10.1002/(SICI)1097-0169(1996)35:3<269::AID-CM8>3.0.CO;2-3.